

# A Remote Sensing Algorithm for Vertically-Resolved Cloud Condensation Nuclei Number Concentrations from Airborne/Spaceborne Lidar Observations

Piyushkumar N. Patel<sup>1,2,\*</sup>, Jonathan H. Jiang<sup>1</sup>, Ritesh Gautam<sup>3</sup>, Harish Gadhavi<sup>4</sup>, Olga V. Kalashnikova<sup>1</sup>, Michael J. Garay<sup>1</sup>, Lan Gao<sup>5</sup>, Feng Xu<sup>5</sup>, Ali H. Omar<sup>6</sup>

<sup>1</sup>Jet Propulsion Laboratory, California Institute of Technology, Pasadena, CA, USA

<sup>2</sup>Oak Ridge Associated Universities, Oak Ridge, TN, USA

<sup>3</sup>Environmental Defense Fund, Washington, DC, USA

<sup>4</sup>Physical Research Laboratory, Ahmedabad, India

<sup>5</sup>School of Meteorology, University of Oklahoma, OK, USA

<sup>6</sup>Science Directorate, NASA Langley Research Center, Hampton, VA, USA

**\*Corresponding Author:** Piyushkumar N. Patel, ([piyushether@gmail.com](mailto:piyushether@gmail.com), [piyushkumar.n.patel@jpl.nasa.gov](mailto:piyushkumar.n.patel@jpl.nasa.gov))

**Keywords:** CCN, aerosol, cloud, CALIPSO, satellite, Lidar, airborne, spaceborne

**Abstract.** Cloud condensation nuclei (CCN) are mediators of aerosol-cloud interactions (ACI), contributing to the largest uncertainties in the understandings of global climate change. We present a novel remote sensing-based algorithm that quantifies the vertically-resolved CCN number concentrations ( $N_{CCN}$ ) using aerosol optical properties measured by a multiwavelength lidar. The algorithm considers five distinct aerosol subtypes with bimodal size distributions. The inversion used the look-up tables developed in this study, based on the observations from the Aerosol Robotic Network to efficiently retrieve optimal particle size distributions from lidar measurements. The method derives dry aerosol optical properties by implementing hygroscopic enhancement factors to lidar measurements. The retrieved optically equivalent particle size distributions and aerosol type dependent particle composition are utilized to calculate critical diameter using the  $\kappa$ -Köhler theory and  $N_{CCN}$  at six supersaturations ranging from 0.07% to 1.0%. Sensitivity analyses indicate that uncertainties in extinction coefficients and relative humidity greatly influence the retrieval error in  $N_{CCN}$ . The potential of this algorithm is further evaluated by retrieving  $N_{CCN}$  using airborne lidar from the NASA ORACLES campaign and validated against simultaneous measurements from the CCN counter. The independent validation with robust correlation demonstrates promising results. Furthermore, the  $N_{CCN}$  has been retrieved for the first time using a proposed algorithm from spaceborne lidar - Cloud-Aerosol Lidar with Orthogonal Polarization (CALIOP) - measurements. The application of this new capability demonstrates the potential for constructing a 3D CCN climatology at a global scale, which help to better quantify ACI effects and thus reduce the uncertainty in aerosol climate forcing.

## 1 Introduction

The Intergovernmental Panel on Climate Change (IPCC) report states that radiative forcing caused by aerosol-cloud interactions (ACI), dominates the largest uncertainty, and remains the least well-understood anthropogenic contribution to climate change (IPCC AR5, 2013). The uncertainty mainly stems from the complicated processes of how aerosols impact the global cloud system. Atmospheric aerosols allow for water vapor condensation under certain supersaturation (SS) conditions and subsequently evolve into cloud droplets by serving as cloud condensation nuclei (CCN). Anthropogenic emissions are a major source of CCN, facilitating the formation of cloud droplets, thereby altering cloud properties, precipitation patterns, and hence the climate forcing (Carslaw et al., 2010; Paasonen et al., 2013). Consequently, reducing the uncertainty associated with ACI is crucial for increasing our confidence in predictions of global and regional climate models (IPCC, 2014). The fundamental parameter for understanding the aerosol-cloud interaction is the CCN concentrations (Rosenfeld et al., 2014). Determining CCN number concentration ( $N_{CCN}$ ) is the basis for analyses of ACI (Seinfeld et al., 2016). Large uncertainties in their magnitude and variability at a global scale are one of the main factors for the low level of scientific understanding of ACI effects. Therefore, knowledge of the global abundance of aerosols capable of serving as CCN is fundamental to advancing our understanding of ACI (Fan et al., 2016).

Tackling the challenges in climate change, as identified by the IPCC, requires that CCN properties be measured globally. Missing such a fundamental quantity has greatly hindered our ability to accurately quantify the effects of anthropogenic aerosols on cloud properties (Rosenfeld et al., 2014). Ground-based instruments can observe  $N_{CCN}$  at various SS, but they only provide sparse and localized information. Besides limited coverage, near-surface CCN properties could differ significantly from CCN properties near the cloud base due to vertical aerosol inhomogeneities, particularly under stable atmospheric boundary conditions. Airborne observations can provide very useful CCN measurements near cloud base but are expensive to collect and are limited to a few field experiments, and having limited spatial-temporal coverage (Feingold et al., 1998; Li, Liu, et al., 2015; Li, Yin, et al., 2015).

Overall, observations of CCN are spatiotemporally sparse, lack the vertical dimension, and provide insufficient constraints on their global distribution. ACI studies often use satellite retrievals to take advantage of their global coverage, but satellites have been unable to measure the CCN. Nevertheless, the aerosol optical parameters such as aerosol optical depth (AOD) and aerosol index (AI) are commonly used as proxies for CCN in previous studies (Gryspeerd & Stier, 2012; Patel et al., 2017, 2019; Patel & Kumar, 2016; Quaas et al., 2008, 2009; Rosenfeld, 2008). However, all these proxies are crude tools and suffer from various issues such as aerosol swelling, lack of vertical information, cloud contamination, uncertainty in size distribution and solubility, and more (Rosenfeld et al., 2016). The aforementioned studies based on passive satellite remote sensing measurements, such as AOD and AI have limitations in several areas for ACI studies.

Active remote sensing technologies such as lidar have the ability to improve the precision and range of conditions under which particle concentrations and their ability to act as CCN can be retrieved. A significant body of prior studies has assessed the relationship between aerosol optical

properties and CCN based on local in situ data offered by lidar and radar. Feingold et al., (1998) developed a technique to derive CCN from the retrieved cloud droplet concentration, vertical velocity, and lidar backscatter from ground-based radar, lidar, and radiometer. Ghan et al., (2006) and Ghan & Collins, (2004) evaluated the relationship between aerosol extinction from airborne lidar and  $N_{CCN}$  from near-surface measurements and devised a technique for estimating CCN at a cloud base. However, their techniques rely on the assumption that the physiochemical characteristics of aerosols at the surface represent the vertical column. Thus, their retrievals may be subject to large uncertainties due to vertical inhomogeneity in particle characteristics. Previous work by Clarke & Kapustin, (2010); Kapustin et al., (2006); Liu & Li, (2014); Shinozuka et al., (2015) demonstrated a strong correlation between extinction coefficients and  $N_{CCN}$  instead of vertically integrated AOD or AI using airborne and in situ observations. Stier, (2016) provided a global assessment of the link between aerosol radiative properties and CCN using a global aerosol-climate model (ECHAM-HAM) and suggested that vertically integrated aerosol radiative properties are of limited suitability as a proxy for global surface CCN.

Both Mamouri and Ansmann, (2016) and Choudhury and Tesche, (2022) examine the potential of single wavelength lidar observations to retrieve CCN number concentrations for different aerosol types. The relationships between particle extinction coefficients and number concentrations of particles with a dry radius larger than 50 nm (for non-dust) and 100 nm (for dust) were parameterized based on multiyear AERONET observations for different aerosol types. However, the measurements from the single wavelength lidar also lack sufficient information to quantify particle size distribution, particle number concentration or aerosol type, resulting in large uncertainty in  $N_{CCN}$  retrieval (Burton et al., 2012; Tan et al., 2019). However, few recent studies (Lv et al., 2018; Tan et al., 2019) have shown efforts to retrieve  $N_{CCN}$  based on the advanced capability of multiwavelength lidar measurements, but they have been limited to ground-based observations only. Rosenfeld et al., (2016) have attempted a new approach to retrieve satellite based  $N_{CCN}$  using passive satellite observations. All these studies taken together provide a sound foundation of CCN-relevant aerosol properties, but most of them do not refer to CCN concentrations themselves, and the ones who do, do not give a global coverage nor a vertically resolved picture. Consequently, no reliable global observational data set of CCN exists, and the ability to routinely measure vertically resolved CCN to study ACI effectively is still lacking (Burkart et al., 2011).

This study introduces ECLiAP (*Estimation of CCN using Lidar measured Aerosol optical Properties*), a comprehensive remote sensing algorithm designed to estimate the concentration of cloud condensation nuclei ( $N_{CCN}$ ) using multiwavelength spaceborne lidar measurements.

This paper is structured as follows: The introductory section discusses the importance and motivation behind  $N_{CCN}$  estimation. Section 2 describes the LUT-based approach utilized for  $N_{CCN}$  estimation, focusing specifically on satellite observations. Section 3 encompasses numerical simulations, sensitivity analysis, extensive validation efforts, and an observational case study. Finally, Section 4 comprehensively discusses the results and their broader implications.

## 2 Dataset

### 2.1 NASA ObseRvations of Aerosols above CLOUDs and their intERactionS (ORACLES)

The NASA ObseRvations of Aerosols above CLOUDs and their intERactionS (ORACLES) campaign, conducted between 2016 and 2018 over the southeast Atlantic (SEA) (Redemann et al., 2021), provided valuable insights into a crucial region characterized by the interaction of biomass burning emissions with marine stratocumulus clouds specifically during July to October. These clouds wield significant influence over global climate; however, climate models often inadequately represent them due to their abundance and brightness (Bony & Dufresne, 2005; Nam et al., 2012). Furthermore, the challenges of non-polarimetric passive remote sensing of aerosols in the presence of low stratocumulus clouds (Chang et al., 2021; Coddington et al., 2010) underscore the criticality of accurately predicting Cloud Condensation Nuclei (CCN) concentrations and refining model parameterization for the SEA region. To address the knowledge gaps, the ORACLES campaign focused on comprehensive observations of aerosol and cloud properties, employing a combination of remote sensing and in situ instruments aboard the NASA P-3 (operational from 2016 to 2018) and ER2 (operational in 2016) aircraft. The ORACLES data includes in-situ measurements of  $N_{CCN}$  from the CCN counter, as well as lidar measurements obtained through NASA Langley Research Center’s high-spectral resolution lidar (HSRL-2). We seized this opportunity to conduct a validation exercise based on the accessible data.

#### 2.1.1 High-Spectral Resolution Lidar (HSRL)-2

The NASA Langley Research Center HSRL-2 measures aerosol backscatter and depolarization at three wavelengths (355 nm, 532 nm, and 1064 nm) and aerosol extinction at 355 nm and 532 nm using the HSRL technique (Burton et al., 2018; Shipley et al., 1983). At 1064 nm, extinction is derived from the product of aerosol backscatter at 1064 nm and an inferred lidar ratio at 1064 nm. The HSRL-2 measurement technique differentiates between aerosol and molecular returns by analyzing the spectral distribution of the return signal. Consequently, this enables the independent determination of aerosol backscatter and extinction coefficients, unlike traditional elastic backscatter lidar retrievals that rely on a lidar ratio assumption (Hair et al., 2008). The addition of the 355 nm channel in HSRL-2 enhances sensitivity to smaller particles, including CCN, which are crucial in aerosol-cloud interactions (Burton et al., 2018). The instrument achieves horizontal and vertical resolutions of approximately 2 km and 15 m, respectively, for aerosol backscatter and depolarization. For aerosol extinction coefficients, horizontal and vertical resolutions are approximately 12 km and 300 m, respectively, with interpolation to match the finer resolutions of backscatter and depolarization. In terms of temporal resolution, aerosol backscatter and extinction coefficients are available at approximately 10 s and 60 s intervals, respectively. The uncertainty in lidar observables, influenced by factors like contrast ratio and aerosol loading, can be within 5% under certain conditions (Burton et al., 2018). This manuscript delves the ability of ECLiAP by leveraging the advanced capabilities of HSRL-2, in accurately deriving  $N_{CCN}$  in the real-world atmospheric conditions.

### 2.1.2 CCN counter

We utilize the Georgia Institute of Technology (GIT) Droplet Measurement Technologies (DMT) CCN counter (CCN-100) as another primary instrument and data source. The CCN-100 facilitates in situ measurements of CCN concentration across a range of water vapor supersaturation levels (S), specifically between 0.1% and 0.4% (Kacarab et al., 2020; Redemann et al., 2021). The CCN-100 is ingeniously designed as a continuous-flow streamwise thermal-gradient chamber (CFSTGC) following the framework proposed by Roberts & Nenes, (2005). In this configuration, a cylindrical flow chamber generates quasi-uniform supersaturation at its centerline through continuous heat and water vapor transport from the wetted walls, subject to a temperature gradient. The difference in heat and water vapor diffusivity in the radial direction ensures the generation of supersaturation at varying levels depending on the flow rate and temperature gradient. An advantage of the continuous-flow system is its rapid sampling capabilities, achieving a frequency of approximately 1 Hz (Roberts & Nenes, 2005). Such high frequency is crucial for effectively capturing rapidly changing environments, typical of airborne sampling scenarios. Aerosols that activate into droplets with a radius greater than  $0.5\ \mu\text{m}$  are counted as CCN at the end of the growth chamber. The horizontal resolution of in situ observations during the ORACLES campaign is contingent upon aircraft speed. For accuracy, the uncertainty associated with CCN number concentration is approximately  $\pm 10\%$  at high signal-to-noise ratio (S/N), while the supersaturation uncertainty is around  $\pm 0.04\%$  (Rose et al., 2008). These precision values assure the reliability of the CCN measurements, ensuring the robustness of the dataset used to validate the ECLiAP derived  $N_{\text{CCN}}$  in our investigation.

## 2.2 Cloud-Aerosol Lidar and Infrared Pathfinder Satellite Observations (CALIPSO)

The CALIOP (Cloud-Aerosol Lidar with Orthogonal Polarization) on the CALIPSO satellite, the first spaceborne polarization lidar, was launched in April 2006 (Winker et al., 2007). CALIPSO is in 705 km sun-synchronous polar orbit, and the orbit is controlled to repeat the same ground track every 16 days with cross-track errors of less than  $\pm 10$  km. CALIOP acquires high-resolution (vertical and horizontal at 30 and 333 m below 8.2 km, and 60 and 1000 m between 8.2 and 20.2 km) profiles of total attenuated backscatter by aerosols and clouds at 532 and 1064 nm during both day and night. Spatial averaging over different scale is typically performed to improve the signal-to-noise ratio for reliable retrievals. For our study, we used the CALIPSO version 4.20 level 2 aerosol profile product (vertical and horizontal resolution:  $60\text{ m} \times 5\text{ km}$ , temporal resolution: 5.92 s). The CALIOP first classified the aerosol and cloud layers using Cloud-Aerosol Discrimination (CAD) score algorithm (Liu et al., 2009). Further, the aerosol layers categorize into the subsequent aerosol types (Omar et al., 2009). The hybrid extinction retrieval algorithms is used to retrieve the aerosol extinction, using the assumed lidar ratios appropriate for each aerosol type (Young & Vaughan, 2009) reported in the CALIPSO level-2 5 km aerosol profile product (Vaughan et al., 2017). The determination of lidar ratio contributes the major uncertainty in the retrieval of CALIOP aerosol extinction, and the misclassification of aerosol type is another source of uncertainty (Yu et al., 2010). We incorporate the profiles of aerosol extinction coefficient,

backscatter coefficient, and particle depolarization ratio, along with aerosol subtype information from CALIOP, into the ECLiAP for the  $N_{CCN}$  retrieval. Additionally, we utilize relative humidity profiles obtained from the Global Modelling and Assimilation Office Data Assimilation System (Molod et al., 2015), which are included in the CALIPSO data product. We employed CALIOP data to assess the  $N_{CCN}$  retrieval capability of ECLiAP and also conducted a case study.

## 3 Methodology

### 3.1 Construction of Lookup Tables

The inversion solution using the combination of simultaneous measurements of backscatters at three wavelengths and extinction at two wavelengths, also called  $3\beta+2\alpha$ , using lidar has been gaining prominence for aerosol microphysical (effective radius, total number, volume concentration, refractive index) retrieval (Burton et al., 2016; Müller et al., 1999, 2005, 2016; Veselovskii et al., 2002, 2004, 2012). Several fundamental aspects of the mathematical problem must be solved during the retrieval from multiwavelength lidar. The most important aspect is that the inversion solution is not unique. The non-uniqueness of an inversion solution in the advanced  $3\beta+2\alpha$  technique is the primary source of the retrieval challenges (Chemyakin et al., 2016). Additionally, retrieving six size parameters (number concentrations, effective radius, and geometric standard deviation for fine and coarse mode particles) for a bimodal particle size distribution (PSD) from five known quantities ( $\beta_{355}$ ,  $\beta_{532}$ ,  $\beta_{1064}$ ,  $\alpha_{355}$ ,  $\alpha_{532}$ ) is still an ill-posed inversion problem. Besides, the existing spaceborne lidar instrument (CALIOP onboard CALIPSO) provides the measurements at only two wavelengths (532 nm & 1064 nm). Considering all these constraints and partially compensating for the non-uniqueness problem, we employed the LUT approach with a fine step of bimodal particle size distributions (PSDs) to derive aerosol size parameters. The parameterization of bimodal lognormal PSD is described in section 2.1.1. The fundamental design of the LUTs framework for lidar measurements builds to test the aerosol optical properties that we target for precise information.

In the present study, the LUTs are designed using the  $3\beta+3\alpha$  ( $\beta_{355}$ ,  $\beta_{532}$ ,  $\beta_{1064}$ ,  $\alpha_{355}$ ,  $\alpha_{532}$ ,  $\alpha_{1064}$ ) technique for the individual aerosol types. An additional input at a longer wavelength improves the retrieval accuracy for coarse mode particles (Lv et al., 2018). These LUTs contain aerosol optical properties such as backscatter coefficients at 355, 532, and 1064 nm ( $\beta_{355}$ ,  $\beta_{532}$ ,  $\beta_{1064}$ ) and extinction coefficients at 355, 532, and 1064 nm ( $\alpha_{355}$ ,  $\alpha_{532}$ ,  $\alpha_{1064}$ ), along with size parameters including number concentration, effective radius and geometric standard deviation for fine and coarse mode particles ( $N_{ff}$ ,  $r_f$ ,  $\sigma_f$ ,  $N_{lc}$ ,  $r_c$ ,  $\sigma_c$ ). Primarily, the LUTs are generated for the five distinct aerosol subtypes: marine, dust, polluted continental, clean continental, and smoke aerosols (as shown in Figure 1). This study considers dust particles to be spheroid, while other aerosol types to be spheres. The particle optical properties are computed using the well-known Mie scattering theory (Bohren & Huffman, 1998) for spherical particles, which is a numerically accurate approach over a wide range of particle sizes. Meanwhile, the T-Matrix method (Mishchenko & Travis, 1998)

is adopted for the spheroids, which is numerically precise for the limited particle sizes. Consequently, the improved geometric optics method (IGOM; Bi et al., 2009; Yang et al., 2007) is applied to the larger spheroids not covered by the T-matrix method. The axis ratio distribution for spheroids, ranging from ~0.3 (flattened spheroids) to ~3.0 (elongated spheroids) is taken from Dubovik et al., (2006). The transition from the TMM to IGOM is determined by specific size parameters and is dependent on the particle shape and refractive index. However, the present study considers the mean complex refractive index, the transition from TMM to IGOM depends on the particle shape. PSD and mean complex refractive index were used as the input parameters for the computations of aerosol optical properties. The parameter ranges for the bimodal size distribution and mean complex refractive index of five aerosol subtypes are presented in Table 1 which are used to construct the respective look-up tables (LUTs). These parameter values were adopted from Dubovik, (2002); Torres et al., (2017) and Veselovskii et al., (2004), who used measurements from sun-sky radiometers at multiple AErosol RObotic NETwork (AERONET) sites. Torres et al., (2017) validated their models against 744 AERONET observations and 165 almucantar AERONET standard inversions at eight different sites. This approach ensures the robustness and reliability of our aerosol characterization. The PSDs are given in terms of the total particle number concentration, effective radius ( $r$ ), and geometric standard deviation individually for fine and coarse modes. Considering the sensitivity limitation of lidar measurements, the range of radius for the PSD is constrained to 0.01-10  $\mu\text{m}$  with a fixed bin size of 0.002 defined on a logarithmic-equidistant scale in the calculation. In the process of constructing LUTs, specific intervals for the parameters  $\sigma_f, \sigma_c, r_f$  and  $r_c$  have been carefully chosen to define the range of particle size distributions for each aerosol model. These intervals are set at 0.01, 0.01, 0.002 and 0.01  $\mu\text{m}$ , respectively. These intervals are set as a compromise between accuracy and computation time, ensuring that the LUTs encompass a comprehensive range of particle size distributions for various aerosol subtypes found in the real atmosphere. Further details on the parameterization of the bimodal particle size distribution is discussed in the subsequent section.

### 3.1.1 Lognormal Aerosol Size Distributions

An earlier study by Kolmogorov, (1941) mathematically proved that the random process of sequential particle crushing leads to a lognormal distribution of particle size. In our study, PSDs have been treated as a bimodal lognormal distribution, as widely used in aerosol remote sensing studies (Dubovik et al., 2011; Remer et al., 2005; Schuster et al., 2006; Torres et al., 2014). Although particle size distributions are not always bimodal in each case, their size distributions can be considered as a combination of fine and coarse modes. This bimodal lognormal size distribution can be expressed as:

$$\frac{dn(r)}{d \ln(r)} = \sum_{i=f,c} \frac{N_{ti}}{(2\pi)^{1/2} \ln \sigma_i} \exp \left[ -\frac{(\ln r - \ln r_i^n)^2}{2(\ln \sigma_i)^2} \right] \quad (1)$$

where  $N_{ti}$  is the total particle concentration of the  $i^{\text{th}}$  mode and  $r_i^n$  is the median radius for the aerosol size distribution, with  $n$  representing the number concentration distribution. The index  $i =$

$f, c$  refers to the fine and coarse modes, respectively. The term  $\ln \sigma_i$  is the mode width of the  $i^{th}$  mode. This general bimodal lognormal size distribution shape for aerosol is adopted in this study to improve the accuracy of the CCN retrieval. The sensitivity assessment regarding the response of CCN to the assumption of bimodal size distributions is presented in section 3.1. For individual lognormal components, the relationships between the volume and number distribution parameters representing by the following equations (Hatch & Choate, 1929):

$$r^n = r^v / \exp[3(\ln \sigma)^2] \quad (2)$$

$$V_t = N_t \frac{4\pi}{3} (r^n)^3 \exp \left[ \frac{9}{2} (\ln \sigma)^2 \right] \quad (3)$$

where,  $V_t$  is the particle volume concentration and  $r^v$  is the median radius for the aerosol volume size distribution. As shown in Figure 1 and Table 1, the main difference between the aerosol subtype is the ratio of the volume concentration of the fine mode to the coarse mode.

### 3.2 Retrieval of CCN Number Concentrations

Building upon the methodology proposed by (Lv et al., 2018), we have enhanced and generalized the approach to enable its application to airborne and spaceborne lidar measurements for CCN estimation. The core of the algorithm relies on the utilization of look-up tables (LUTs) that incorporate aerosol size and composition information, facilitating reliable and vertically-resolved CCN estimation.  $N_{CCN}$  values are obtained at six critical supersaturations from 0.07% to 1.0% based on retrieved particle size distributions. Significant improvements have been implemented within the methodology. Firstly, its applicability has been expanded to accommodate lidar measurements from diverse platforms. Secondly, the LUTs now include five aerosol types, ensuring a more comprehensive representation of aerosol characteristics. Thirdly, the methodology leverages the additional signal of the extinction coefficient at 1064 nm, effectively addressing the uncertainty associated with the non-uniqueness problem during the inversion process. Fourthly, including the hygroscopic growth correction in the revised method has led to significant improvements in the accuracy of CCN estimation, further enhancing the reliability and robustness of the. Finally, results the extensive analysis has been conducted by including the errors from RH.

This section discusses a detailed methodology adopted by ECLiAP to retrieve  $N_{CCN}$  from the given lidar measurements.

#### 3.2.1 Overview

An optically related  $N_{CCN}$  is introduced to bridge the gap between aerosol particle and their activation capability to serve as a cloud droplet. The ability of particles to act as CCN is mainly controlled by particle size distribution followed by chemical composition (Dusek et al., 2006; Patel & Jiang, 2021). However, both factors are significant in specific regions (Mamouri & Ansmann, 2016). Therefore,  $N_{CCN}$  could be quantified with size distribution and compositional



information. The key feature of an approach adopted in ECLiAP is to seek the parameters that can provide the size and composition of particles consistent with lidar measurements under dry conditions and use these parameters to estimate  $N_{CCN}$ .

Figure 2 illustrates a schematic diagram of the method to retrieve  $N_{CCN}$  from satellite observations.

In the natural environment, the particle hygroscopic properties influence the particle size distribution and their optical properties, especially when it is near a cloud base or under a high moist environment. Therefore, the lidar measured aerosol optical properties under ambient conditions need to be corrected to the dry aerosol optical properties using the hygroscopic enhancement factor. The hygroscopic enhancement factor can be fitted by the parameterization scheme using enhancement of backscatter and extinction coefficients with RH. Particle dry backscatter and extinction can also be inferred from the hygroscopic enhancement factor. An approach to computing hygroscopic enhancement factors and performing hygroscopic correction to obtain dry backscatter and extinction is described in Section 2.2.2. This step is applied to all the  $3\beta+3\alpha$  parameters before looking for aerosol size parameters from the LUT. Before applying hygroscopic correction, lidar-measured optical properties, particularly for dust mixtures (polluted dust and dusty marine), are separated into dust and non-dust components using the backscatter coefficients and particle depolarization ratio (Teschke et al., 2009). The methodology to separate the dust mixture is discussed in Appendix A1. The resulting dust and non-dust aerosol optical properties, along with aerosol subtype and relative humidity, is then utilized in the ECLiAP algorithm (as shown in Figure 2) to estimate CCN concentrations. Note that the direct inclusion of internal mixtures in our analysis and LUTs poses complexity and challenges. As a result, our approach primarily centers on studying and analyzing external mixtures of aerosol subtypes.

Once the dry aerosol optical properties are derived, an ECLiAP look for the suitable size parameters from the LUTs for the given dry aerosol optical properties and respective aerosol subtype (see section 2.2.3). As mentioned earlier, the ability of particles to act as CCN is mainly controlled by particle size distribution followed by chemical composition. Deriving composition information of particles from the lidar measurements is not yet well-defined. Therefore, in the absence of chemical composition data, mean chemical composition information denoted by a single value of  $\kappa$ , the so-called hygroscopicity parameter, is achievable for estimating  $N_{CCN}$ , which describes the relationship between the particle dry diameter and CCN activity. The sensitivity of the estimated  $N_{CCN}$  to  $\kappa$  depends strongly on the variability of the shape of the aerosol size distribution (Wang et al., 2018). Therefore, the chemical information becomes less important in estimating  $N_{CCN}$ , especially (Patel & Jiang, 2021) Jiang, 2021). Most studies reported that the uncertainty of using the mean value of  $\kappa$  to estimate the  $N_{CCN}$  is less than 10% (Jurányi et al., 2010; Wang et al., 2018), which varies with atmospheric conditions. In ECLiAP, the literature values of  $\kappa$  are considered for each aerosol subtype for further retrieval. The  $\kappa$  is assumed to be 0.7 for marine (Andreae & Rosenfeld, 2008), 0.03 for dust (Koehler et al., 2009), 0.27 for polluted continental (Liu et al., 2011), 0.3 for clean continental (Andreae & Rosenfeld, 2008), and 0.1 for smoke aerosols (Petters et al., 2009) for the later computations.

Finally, an ECLiAP uses the retrieved optically equivalent size parameters from LUTs and  $\kappa$  value as composition information for the further computation of critical radius using the  $\kappa$ -Köhler theory (Petters & Kreidenweis, 2007), and hence the  $N_{CCN}$  for the six fixed supersaturations (see section 2.2.4). For the dust mixture,  $N_{CCN}$  derived separately both for dust and non-dust are added lastly.

### 3.2.2 Separation of optical properties for dust mixture

We have adopted the methodology by Tesche et al., (2009) to separate the dust and non-dust extinction coefficients in the dust mixtures (polluted dust and dusty marine) using particle backscatter coefficients and particle depolarization ratio. The optical properties

$$\beta_d = \beta_p \frac{(\delta_p - \delta_2)(1 + \delta_1)}{(\delta_1 - \delta_2)(1 + \delta_p)} \quad (A1.1)$$

This study incorporates wavelength-dependent depolarization ratios  $\delta_1$  and  $\delta_2$  to distinguish the dust and non-dust aerosol components. The reported particle depolarization ratio from various campaigns is listed in the Table S1. In this study, mean values of  $\delta_1$  (0.24, 0.31 and 0.06) and  $\delta_2$  (0.03, 0.05, and 0.02) at 355, 532 and 1064 nm, respectively, are utilized. If the measured depolarization ratio  $\delta_p > \delta_1$  ( $< \delta_2$ ) then aerosol mixture is considered as pure dust (non-dust). For remaining  $\delta_p$  values, we first estimate  $\beta_d$  using the above equation and then calculate  $\beta_{nd}$  by subtracting  $\beta_d$  from  $\beta_p$ . Subsequently, the extinction coefficients are computed by multiplying the backscatter coefficients with the respective lidar ratio. Determining a spatially varying lidar ratio for dust across different regions presents challenges due to uncertainties in identifying dust source regions during transport. Therefore, we employ a simplified approach using a single lidar ratio value. Previous studies have reported little to no wavelength dependency of lidar ratio for dust and marine aerosol based on ground-based Raman lidar and airborne HSRL lidar measurements. As a result, we consider a constant lidar ratio of 44 for dust and 23 for marine to calculate the extinction coefficients at the three wavelengths. However, for polluted continental aerosols, we utilize wavelength-dependent lidar ratios of 58, 70 and 30 at 355, 532 and 1064 nm (Giannakaki et al., 2016; Hänel et al., 2012; Kim et al., 2018; Komppula et al., 2012; Müller et al., 2007).

### 3.2.3 Derivation of dry backscatter and dry extinction

It is difficult to measure the complex chemical composition and associated water uptake capability of a particle with increasing RH. Therefore, a widely popular and simple parameterization scheme was used to describe the changes in aerosol optical properties with atmospheric RH relative to a dry (or low-RH) state, also called the hygroscopic enhancement factor. Recent aerosol hygroscopic studies (Bedoya-Velázquez et al., 2018; Fernández et al., 2018; Lv et al., 2017) have derived backscatter and extinction enhancement factors using lidar measurements and RH profiles. The hygroscopic enhancement factor that is associated with both particle size and hygroscopicity (Kuang et al., 2017), is defined as:

$$f_{\xi}(RH, \lambda) = \frac{\xi(RH, \lambda)}{\xi(RH_{dry}, \lambda)} \quad (4)$$

where  $f_{\xi}$  is the hygroscopic enhancement factor of the optical property  $\xi$  (backscatter and extinction) at a specific light wavelength  $\lambda$  and RH, and  $RH_{dry}$  is the reference RH value (RH=0). There is no generic reference RH that represents the dry conditions for lidar measurements, unlike in-situ controlled RH measurements, to derive enhancements factor. Inferring dry backscatter and extinction coefficients is also crucial in CCN retrieval. Therefore, parameterization of the hygroscopic growth of lidar-derived optical properties should combine dry aerosol optical properties and  $f_{\xi}(RH, \lambda)$  together. Previous studies have proposed several parameterization schemes for hygroscopic enhancement factors (Titos et al., 2016). The most frequently used parameterization scheme is a power-law function that is known as gamma parameterization, introduced by Kasten, (1969):

$$f_{\xi}(RH, \lambda) = A \cdot (1 - RH/100)^{-\gamma} \quad (5)$$

Where the parameter A gives the extrapolated value at RH=0% and the exponent  $\gamma$  is the fitting parameter and defines the hygroscopic behavior of the particles. Recently, a new physically based single-parameter representation approach was proposed by Brock et al., (2016) to describe the hygroscopic enhancement factor. Their results claimed that this proposed parameterization scheme better describes light-scattering hygroscopic enhancement factors than the widely used gamma power-law approximation. The formula of this new scheme is written as:

$$\xi(RH, \lambda) = \xi_{dry}(RH, \lambda) \cdot f_{\xi}(RH) = \xi_{dry}(RH, \lambda) \cdot \left[ 1 + \kappa_{\xi}(\lambda) \frac{RH}{100 - RH} \right] \quad (6)$$

where,  $\kappa_{\xi}$  is a dimensionless fitting parameter and shows a significant correlation with bulk hygroscopic parameter  $\kappa$ ; but they are not equivalent (Brock et al., 2016; Kuang et al., 2017).  $\xi_{dry}$  denotes dry aerosol optical properties (backscatter and extinction coefficients).

For the estimation of the hygroscopic enactment factor, aerosol optical properties (backscatter and extinction coefficients) at 355, 532, and 1064 nm are calculated over a range of RH (0-99%) using Mie theory (T-matrix and IGOM for spheroid) for the range of PSDs and each aerosols subtype. Figure S1 illustrates the mean curve of the hygroscopic enhancement factor (the ratio between the aerosol optical properties at specific RH to dry RH) at three wavelengths with increasing RH for each aerosol subtype. With given aerosol optical properties at different RHs,  $\kappa_{\xi}$  can be fitted by curve fitting using Eq. (6). However, Tan et al., (2019), based on a comparison of  $\kappa_{\xi}$  and derived  $\xi_{dry}$  for various ranges of RH, showed that the fitting hygroscopic parameters are found to be sensitive to fitting RH range when the RH range is limited and relatively high (between 60% and 90%). Therefore, we fixed the RH range to 60%-90% for the parameter fitting (highlighted curve in Figure S1). In addition, retrieving finite dry aerosol optical properties could not be possible for

the observation with  $RH > 99\%$ . Therefore, ECLiAP only applies the hygroscopic correction when  $RH$  is between 40% and 99%. In ECLiAP, individual  $\kappa_\xi$  values for each aerosol optical property at three different wavelengths, along with the  $RH$  value, are used to obtain the dry aerosol optical properties separately for each aerosol subtype using Eq. (6).

### 3.2.4 Inversion techniques for size parameters

ECLiAP utilizes an inverse approach, distinct from traditional methods, to estimate the particle size distribution from Look-Up Tables (LUTs) using lidar inputs. This process involves inferring particle size distribution from known aerosol optical properties, determining the best-fitting solution that corresponds to the observed lidar measurements. It differs from the traditional  $3\alpha+2\beta$  technique typically used for inversion.

Once the dry aerosol optical properties are obtained, the ECLiAP searches for suitable size parameters from the LUTs. For this, the ECLiAP look for the best combination of six values ( $N_{tf}$ ,  $r_f$ ,  $\sigma_f$ ,  $N_{tc}$ ,  $r_c$ ,  $\sigma_c$ ) to match inputs ( $\beta_{355}$ ,  $\beta_{532}$ ,  $\beta_{1064}$ ,  $\alpha_{355}$ ,  $\alpha_{532}$ ,  $\alpha_{1064}$ ) by minimizing the following function:

$$\mu^{sum} = \sum_{i=1, \dots, 6} \left| \frac{x_i - x'_i}{x_i} \right| \quad (7)$$

Where  $x_i$  represents input aerosol optical data ( $\beta_{355}$ ,  $\beta_{532}$ ,  $\beta_{1064}$ ,  $\alpha_{355}$ ,  $\alpha_{532}$ ,  $\alpha_{1064}$ ) and  $x'_i$  is aerosol optical data ( $\beta'_{355}$ ,  $\beta'_{532}$ ,  $\beta'_{1064}$ ,  $\alpha'_{355}$ ,  $\alpha'_{532}$ ,  $\alpha'_{1064}$ ) derived from LUTs, which are calculated from Mie theory (or T-matrix and IGOM for spheroid) and size distribution parameters.

Each LUT consists of two parts to reduce the dimensions and size of LUTs. Therefore, the particle size distribution, as shown in Eq. (1), can be rewritten as:

$$\frac{dn(r)}{d \ln(r)} = \sum_{i=f,c} \left\{ \frac{1}{(2\pi)^{1/2} \ln \sigma_i} \exp \left[ -\frac{(\ln r - \ln r_i^n)^2}{2(\ln \sigma_i)^2} \right] \cdot N_{ti} \right\} = \sum_{i=f,c} x_i \cdot N_{ti} \quad (8)$$

Where  $x_f$  and  $x_c$  refer to the data bank precomputed with ( $\sigma_f, r_f$  and  $r$ ) and ( $\sigma_c, r_c$  and  $r$ ), respectively. Furthermore, we have adopted the successive approximation method (Kantorovitch, 1939) to deal with the extensive range of  $N_{tf}$  and speed up the finding for the closest solution. Therefore, the inversion technique is further divided into two steps. Step-1: search for an approximate solution based on the criterion in Eq. 8 and calculate the corresponding aerosol optical data ( $\beta'_{355}$ ,  $\beta'_{532}$ ,  $\beta'_{1064}$ ,  $\alpha'_{355}$ ,  $\alpha'_{532}$ ,  $\alpha'_{1064}$ ) from the data banks ( $x_f$  and  $x_c$ ) and  $N_{tf}$  and  $N_{tc}$ . The step widths of  $N_{tf}$  and  $N_{tc}$  are considered to be 100 and  $0.1 \text{ cm}^{-3}$ , respectively. Step 2: based on the approximate solution obtained in step 1, determine the smallest solution space of  $N_{tf}$  by repeating the procedure in step 1 using a smaller step width of  $10 \text{ cm}^{-3}$  for  $N_{tf}$ . Search for the optimal solution of six size parameters ( $N_{tf}$ ,  $r_f$ ,  $\sigma_f$ ,  $N_{tc}$ ,  $r_c$ ,  $\sigma_c$ ).

### 433 3.2.5 Estimation of $N_{CCN}$

434 For the given aerosol optical properties, the retrieved size parameters and the associated  
 435 hygroscopicity parameter ( $\kappa$ ; as discussed in section 2.2.1) were used to calculate the critical  
 436 radius. The critical radius ( $r_{crit}$ ) above which all particles are activated into droplets for a certain  
 437 supersaturation ratio ( $S_c$ ) can be computed from the  $\kappa$ -Köhler theory as suggested by Petters &  
 438 Kreidenweis, (2007):

$$D_{crit} = \left( \frac{4A^3}{27 * \kappa * \ln(S_c)^2} \right)^{1/3}; \quad A = \frac{4\sigma_{s/a}M_w}{RT\rho_w} \quad (9)$$

439 Where,  $D_{crit}$  is the critical diameter ( $r_{crit} = D_{crit}/2$ ), and  $S_c = SS + 1$ ,  $M_w$  and  $\rho_w$  are the  
 440 molecular weight and water density, while R and T are the ideal gas constant and the absolute  
 441 temperature, respectively and  $\sigma_{s/a} = 0.072 \text{ J m}^{-2}$ . The critical radius is determined at six critical  
 442 supersaturations for activation (0.07%, 0.1%, 0.2%, 0.4%, 0.8% and 1.0%). While lidar  
 443 measurements are more sensitive to particles with sizes around 50 nm and larger, this method  
 444 incorporates factors such as particle size distribution, chemical composition, supersaturation  
 445 levels, and thermodynamic properties to estimate the critical radius even for particles below the  
 446 typical lidar sensitivity range.

447 Finally, the ECLiAP calculates  $N_{CCN}$  by integrating size distribution from critical radius to  
 448 maximum radius as:

$$N_{ccn} = \int_{\ln r_c}^{\ln r_{max}} \frac{dn(r)}{d \ln(r)} d \ln(r) \quad (10)$$

449

## 450 4 Results

### 451 4.1 Sensitivity analysis

452 Evaluating the algorithm is a challenging task in the absence of standard and reliable  
 453 measurements. The performance of the ECLiAP is evaluated using numerically simulated  
 454 observations with different error characteristics.

#### 455 4.1.1 Retrieval of $N_{CCN}$ with error-free data

456 To assess the inversion performance and stability ECLiAP, we first performed a sensitivity  
 457 analysis under the assumption of error-free lidar measurements. We used 2000 different sets of  
 458 bimodal size distributions for each aerosol subtypes and used them to simulate the lidar  
 459 observations. The retrieval was repeated to each simulated lidar observations, and the retrieved

size parameters were used to calculate the errors in the retrieved  $N_{CCN}$  ( $N_{CCN}^{ret}$ ) with respect to the initial inputs ( $N_{CCN}^{int}$ ). The errors were calculated as the percentage difference using Eq. 8.

$$CCN\ Error = [(N_{CCN}^{ret} - N_{CCN}^{int})/N_{CCN}^{int}] \times 100\% \quad (11)$$

Table 2 lists the statistical results of CCN error for each aerosol type. As the number shows, the initial  $N_{CCN}$  is well reproduced from the error-free inputs for each aerosol size distribution. The standard deviation of the retrieved CCN errors from the different sets of bimodal size distribution data is also estimated along with the mean value to determine the range of the retrieved CCN error. As mentioned above, the appropriate balance between the accuracy and processing time of the LUTs leads the mean CCN error close to zero but not equal to zero. However, the small standard deviation ( $<0.25$ ) indicates the smaller variances of errors among the aerosol size distributions. Although the high accuracy of LUTs provides the CCN error closer to zero, the calculations are more time expensive. In general, the retrieval results shown in Table 2 exhibit the good accuracy and stability of the inversion algorithm for each aerosol subtype.

Additionally, the sensitivity of the  $N_{CCN}$  retrieval to the assumption of the bimodal size distribution is tested against the aerosol size distribution measurements at the U.S Department of Energy's Atmospheric Radiation Measurement (ARM) climate research facility from the Southern Great Plain (SGP) site. Particle size distribution was measured simultaneously by an Ultra-High Sensitivity Aerosol Spectrometer (for the 0.07 to 1  $\mu m$  geometric diameter range) and an Aerodynamic Particle Sizer (TSI-3321; for the 0.7 to 5  $\mu m$  aerodynamics diameter range). The size conversion factor, defined as the ratio of aerodynamic diameter to geometric diameter, was used to construct a trimodal lognormal particle size distribution. For the purpose of this study, the corresponding bimodal fits are produced, which are representative of the observed size distributions. Figure S2 shows an example of the observed aerosol size distribution and the corresponding bimodal fits. The comparison suggests that bimodal lognormal size distributions can well represent the observed aerosol size distributions qualitatively. Later, we calculate  $N_{CCN}$  based on the bimodal fits and compare them with the 100 observed size distributions to quantify the errors arising from the bimodal lognormal fits. The associated  $\kappa$  values are estimated based on observed PSDs and  $N_{CCN}$  values as described in Patel & Jiang, (2021). The induced CCN errors from the bimodal fitting are shown in Table 3. The absolute value of  $N_{CCN}$  retrieval errors is 3.9%, with a standard deviation of 2.8% at 0.1% supersaturation. Overall, the results suggest that bimodal lognormal aerosol size distributions are adequate for retrieving  $N_{CCN}$ , but errors from the bimodal assumption are not negligible.

#### 4.1.2 Impact of systematic and random errors on $N_{CCN}$ retrieval

Both systematic and random errors exist in lidar-retrieved measurements (Mattis et al., 2016). Systematic errors can be induced by experimental conditions, retrieval algorithms, data processing methods, and our understanding of physical interactions. Sensitivity analysis tests the impacts of systematic errors from backscatter and extinction coefficients on  $N_{CCN}$  retrieval. Although the

systematic errors of different parameters are correlated, the errors are considered independent for individual lidar measurements in the simulations. The error range is reasonable for most current lidar systems. The systematic errors ranging from -20% to 20% with an interval of 5% are applied to one input parameter at a time (others are kept error-free) in each test to understand the impacts on individual parameters better. The inversion algorithm is performed to obtain a new set of aerosol size distributions and retrieve  $N_{CCN}$  data. The procedure is repeated for each input parameter and error value with 200 sets of the randomly generated size distribution for each aerosol subtype. The percentage errors in  $N_{CCN}$  associated with systematic errors can be estimated by comparing retrieved and initial values of  $N_{CCN}$  using Eq. 11. Note that we have also conducted additional simulations for higher range of the error and found that our results are unchanged. However, Pérez-Ramírez et al., (2013) demonstrated that larger errors in the input data can cause significant and unpredictable deviation in the retrieved results. The error range  $\pm 20\%$  is reasonable for most lidar systems.

Figure 3 illustrates the error in retrieved  $N_{CCN}$  as a function of the systematic errors in backscatter and extinction coefficients. The slope of the curve indicates the sensitivity of  $CCN$  errors to systematic errors in individual parameters. A steeper slope infers a high sensitivity in the  $N_{CCN}$  retrieval to the systematic error for a given input parameter. Errors in retrieved  $N_{CCN}$  increase as errors of backscatter and extinction increase, and it is even steeper at higher supersaturations. In general,  $N_{CCN}$  retrievals are most sensitive to errors in extinction coefficients followed by backscatter coefficients. Interestingly, the results are less sensitive to errors in backscatter coefficients at lower supersaturations ( $\leq 0.2\%$ ) but are relatively more sensitive at higher supersaturations ( $> 0.2\%$ ). This indicates that reducing uncertainties in the extinction coefficients can effectively improve the accuracy of  $N_{CCN}$  retrieval while reducing uncertainty in backscatter coefficients can be beneficial for retrieving  $N_{CCN}$  at higher supersaturation. Errors in  $\alpha_{355}$  influence the retrieval results the most. On average, a positive relative error of 20% in  $\alpha_{355}$  overestimates the  $N_{CCN}$  retrieval by about 20% at lower supersaturation and about 50% at higher supersaturation. A negative error of 20% in  $\alpha_{355}$  underestimates the  $N_{CCN}$  retrieval, and the degree of impact is slightly higher than the positive error. Errors in  $\alpha_{532}$  and  $\alpha_{355}$  have the opposite effect on the retrieval error. It is also clear that the influence of systematic errors on the retrieval of  $N_{CCN}$  varies with activation radius, as elucidated by the different signs of the slopes. For instance, the slopes of the extinction coefficient for dust aerosols reverse the sign when the activation radius exceeds low to high supersaturation. These differences most likely result from the reduced retrieval sensitivity to the coarse mode of the aerosol size distribution. In addition, there are substantial distinctions among the types of aerosols. Dust and marine aerosols have the largest absolute errors compared to others dominated by fine-mode particles (see Table 2). These collectively indicate that there are better constraints for fine-mode aerosols than for coarse-mode aerosols, which introduce a larger retrieval error in  $N_{CCN}$  for aerosols with more weight in the coarse mode. It is noteworthy that incorporating an additional input signal of extinction coefficient at 1064 nm in the ECLiAP reduces the error by  $\sim 20\%$  in the coarse mode-dominated aerosol subtypes (dust and marine), and  $\sim 15\%$  in total compared to the previous studies (Lv et al., 2018; Tan et al., 2019).

Nevertheless, integrating an additional lidar signal at a wavelength longer than 1064 nm may further reduce retrieval error for the coarse mode-dominated aerosol type.

RH is another crucial parameter in the present retrieval algorithm for  $N_{CCN}$ . Errors in RH derived by remote-sensing or reanalysis influence the values of growth factors and result in the dry aerosol optical properties, which in turn influence all the input parameters. Therefore, systematic errors ranging from -10% to 10% in intervals of 2% are considered for RH. Figure 4 shows the result of systematic errors in RH. We observed that  $N_{CCN}$  is overestimated when RH has a negative systematic error, and the extent of overestimation in  $N_{CCN}$  increases as the error increase. A negative error of 10% in RH overestimates  $N_{CCN}$  at lower supersaturation by about 20% and doubles (~40%) at higher supersaturation. The effects of the positive errors in RH are relatively smaller and more complicated than negative errors. The mean retrieval error peaked at the RH error at 6%, and the standard deviation of retrieval error increased with the RH error. This suggests that underestimating RH causes large errors than overestimation. Therefore, extra care should be paid to RH measurements if RH-related hygroscopic enhancements of aerosol optical properties are considered.

Systematic errors introduce mean biases in  $N_{CCN}$  retrievals, whereas random errors in observations produce random  $N_{CCN}$  retrieval errors. Random errors obeying Gaussian distributions are produced arbitrarily with a mean value of zero. The standard deviations are set to 10% for aerosol optical properties and to 5%, 10%, and 20% for RH in each test. The simulation is repeated 5000 times for each aerosol subtype, and the statistical results are presented in Figure 5. The mean values of relative error are presented by color, and the number indicates the standard deviation. The error does not change significantly as the random error of RH increases. The mean random errors are relatively small and non-zero, mainly because the sensitivities of  $N_{CCN}$  retrievals are different for different aerosol optical data. The standard deviations are within 16%-28%. The results reveal that random errors in the given input parameters may also contribute to systematic errors in the  $N_{CCN}$  retrievals. The largest mean relative errors are found for coarse mode-dominated aerosol subtypes (dust and marine), consistent with the sensitivities to systematic errors. As discussed earlier, considering additional lidar measurements at longer wavelengths that are more sensitive to larger particles could improve the retrieval of  $N_{CCN}$  for the coarse mode-dominated aerosol subtypes. The mean values of relative errors increase with increasing supersaturation for all aerosol types. Errors in the retrieved  $N_{CCN}$  follow a Gaussian distribution for low supersaturation. However, the Gaussian shape disappears, and the high frequencies shift to the edge of the distribution when supersaturation shifts from low to high (not shown here). Furthermore, the influence of random errors on the individual input parameters is also assessed and is shown in Figure S3. Random errors underestimate the enhancement factor ( $\kappa_\xi$ ) by 30%-40% for 5% RH error, 45%-60% for 10% RH error, and 65%-75% for 20% RH error. The relative errors in  $\beta$  are likely to be overestimated, whereas they are underestimated in  $\alpha$ . The absolute relative error of input parameters becomes larger as the random error of RH grows.



## 4.2 Comparison with airborne measurements

The evaluation of  $N_{CCN}$  retrieval depends on how well retrieved and observed values are matched, as matching errors can become overwhelming. Therefore, we have carried out a validation approach by comparing ECLiAP retrieved  $N_{CCN}$  from lidar measurements with the in-situ measurements of  $N_{CCN}$  by CCN counter during the NASA ORACLES airborne campaign, which occurred from 2016 to 2018 over the Southeast Atlantic (SEA) (Redemann et al., 2021; Zuidema et al., 2016).

HSRL-2 measures the vertical profiles of aerosol optical properties, whereas the CCN counter provides measurements for point location. Therefore, we carried out two strategically different validation exercises in this study: (1) the vertical profile-based comparison and (2) the comparison of collocated measurements. For the profile-based comparison, an ascending path of flight (area covered within the yellow dashed line in Figure S4) on 19 October 2018 has been considered, so the measurements of the CCN counter can be available at various altitudes. Prior to comparison, the lidar measurements from HSRL-2 are averaged over a selected wide space and time (yellow dashed line box in Figure S4). The  $N_{CCN}$  measurements from the CCN counter were available at the supersaturation between 0.32% and 0.34%. Hence, the  $N_{CCN}$  were retrieved at the supersaturation of 0.34% by applying ECLiAP to the mean profiles of lidar measurements. It is noteworthy that the retrieval has been carried out only on those observations having valid lidar measurements at least for two wavelengths. Figure 6a demonstrates the retrieval fit to HSRL-2's vertical dry aerosol extinction coefficient measurements at 355, 532, and 1064 nm. A smoke aerosol dominates the ~93% of profiles at the altitude above 800 meters and marine at lower altitudes (< 800 m), having RH between 30%-105%. The finite dry aerosol optical properties close to the surface could not be retrieved for the observations with RH>99%. The retrieved profiles of dry extinction coefficients are in better agreement with the measured by HSRL-2. This illustrates the ability of the kappa parametrization to account for aerosol hygroscopicity. The vertical mean of absolute fitting error of extinction coefficient is found to be 3.2%, 4.8%, and 6.3% for 355, 532, and 1064 nm, respectively, and the vertical mean of absolute fitting error of backscatter coefficients is 5.1%, 6.7% and 8.9% for 355, 532 and 1064 nm respectively. The fit to the backscatter coefficients of 1064 nm has a relatively larger error. Certainly, one needs to know that the vertically resolved extinction coefficient at 1064 nm is derived using the backscatter coefficient at 1064 nm and lidar ratio. Since HSRL-2 does not directly measure extinction at 1064 nm, it is computed from an assumed relationship with the measured lidar ratio at 532 nm. Though provided as a best guess, such an estimate may cause extra uncertainty to the 1064 nm. Furthermore, the comparison of vertical profiles of ECLiAP retrieved  $N_{CCN}$  from lidar measurements and the  $N_{CCN}$  measured by the CCN counter is shown in Figure 6b. The retrieved values captured the pattern of altitude variations in  $N_{CCN}$  as observed by the in-situ measurements. However, the magnitude of retrieved  $N_{CCN}$  is slightly overestimated by ~12% in total. The overestimation is lower (~9%) at above 2 km, whereas, at below 1 km, it is slightly higher (~16%). A plausible reason behind the relatively large overestimation at below 1 km might be the considerable variation of RH between 60%-105% or/and the highly variable aerosol properties due to the mixture of multiple aerosol

subtypes (smoke, marine, and dust). In addition, wind-driven advection and the age of the air parcel radically modify the characteristics of smoke aerosols and their hygroscopic behavior, which also leads to the slight overestimation of retrieved  $N_{CCN}$  values. The discrepancy between the retrieved and observed values of  $N_{CCN}$  should be reassessed with the robust measurements from the varieties of aerosol subtypes using the multi-campaign airborne data.

The second robust validation exercise is performed, based on collocated measurements, using two years (2017-2018) of combined data from the ORACLES campaign. In 2017-2018, both HSRL-2 and CCN counter were installed on the NASA P-3 flight. The end goal of this exercise is to find one lidar measurement from HSRL-2 to directly compare with one  $N_{CCN}$  measured by the CCN counter, both observed in approximately the same time and space. We defined collocation criteria for any given HSRL-2 profile as follows. The collocation method finds CCN measurement that falls within  $\pm 1.1$  km horizontal distance,  $\pm 60$  m vertical distance, and  $\pm 10$  minutes of the time window. Later, the meteorological parameters within the given space and time windows are extracted along with lidar measurements and measured  $N_{CCN}$  from each flight of the 2017-2018 ORACLES campaign. ECLiAP is applied to each lidar measurement for  $N_{CCN}$  retrieval on the same supersaturation value measured by the CCN counter (lies within the range from 0.2-0.4% SS). Figure 7 represents the result from the comparison of retrieved and measured  $N_{CCN}$ . The  $N_{CCN}$  inferred from the CCN counter measurement is in better agreement with the retrieved  $N_{CCN}$  with a correlation coefficient (R) of  $\sim 0.89$ , a root mean square error (RMSE) value of  $302.8 \text{ cm}^{-3}$ , and a bias of  $138.8 \text{ cm}^{-3}$ . The systematic positive bias in the comparison indicates that the retrieved  $N_{CCN}$  are overestimating the observed values. It is noteworthy that smoke aerosols dominate in the observations from ORACLES, but it also has significant observations from marine, dust, and polluted dust. The discrepancy between measured and retrieved values could be due to the variabilities in the aerosol properties. Overall, the strong correlation in the validation results demonstrates the potential of ECLiAP in retrieving  $N_{CCN}$  from lidar measurements. It recommends having a detailed validation study separate for aerosol subtypes using ground-based and aircraft measurements to evaluate the reliability of the ECLiAP algorithm in estimating the  $N_{CCN}$ .

### 4.3 Retrieving $N_{CCN}$ from spaceborne lidar (CALIOP/CALIPSO): a case study

Extending the scope of ECLiAP, the methodology was converted into a procedure that can be applied to any level-2 aerosol profile dataset from Cloud-Aerosol Lidar with Orthogonal Polarization (CALIOP) on the Cloud-Aerosol Lidar and Infrared Pathfinder Satellite Observations (CALIPSO) (Winker et al., 2007). As an illustrative example, this procedure was applied to a regular CALIPSO track for 01 January 2019 starting at 20:08 UTC, which spans from  $10^\circ\text{N}$  to  $40^\circ\text{N}$ , passing over the Tibetan plateau and Indian landmass. The CALIPSO track (solid black line) can be seen on the right-hand side in Figure 8a. CALIOP onboard CALIPSO provides measurements of aerosol optical properties only at two wavelengths (532 and 1064 nm). Therefore, a total of six parameters ( $\beta_{532}$ ,  $\beta_{1064}$ ,  $\alpha_{532}$ ,  $\alpha_{1064}$ , depolarization ratio, and aerosol subtypes) from CALIOP along with meteorological parameters (RH, temperature) are provided as the inputs to ECLiAP and retrieved total particle concentration ( $N_{CN}$ ) and  $N_{CCN}$  at six supersaturations as

outputs. The  $N_{CN}$  amount represents the total number of aerosol particles that can serve as centers for condensation, while the  $N_{CCN}$  is the fraction of  $N_{CN}$  that can activate as CCN.

The extinction coefficient at 532 nm and aerosol subtypes, along with retrieved  $N_{CN}$  and  $N_{CCN}$  at supersaturation of 0.4%, are shown in Figure 8. Unfortunately, due to the retrieval limitation over the elevated region along with cloudiness, there are no valid aerosol measurements over the Himalayan-Tibetan plateau (as shown by a gap between 28 °N to 37 °N). On the contrary, a strong mixed aerosol signal is observed over the Indian landmass ( $\alpha_{532}$  larger than 2.5 km<sup>-1</sup>), while an elevated (altitude >1 km) dust aerosol layer ( $\alpha_{532} \sim 1.0$  km<sup>-1</sup>) at the edge of the CALIPSO track over the Taklamakan desert (above 38 °N). Over southern India (below 17 °N) polluted continental aerosols prevail ( $\alpha_{532}$  between 0.5-0.8 km<sup>-1</sup>) and mostly accumulate within the boundary layer ( $\sim 1.5$  km a.s.l.), while over northern India (above 19 °N), the aerosol situation includes a mixture of polluted continental and polluted dust ( $\alpha_{532} \sim 1.6$  km<sup>-1</sup> below 1 km altitude). The corresponding vertical cross-section of retrieved  $N_{CN}$  and  $N_{CCN}$  at a supersaturation of 0.4% using ECLiAP can be seen in Figures 8c and 8d, respectively.  $N_{CN}$  and  $N_{CCN}$  larger than 25000 cm<sup>-3</sup> and 3000 cm<sup>-3</sup> at a supersaturation of 0.4% appear over the areas where polluted continental aerosols dominate (southern India), while  $N_{CCN}$  is greater than 2000 cm<sup>-3</sup> appears over northern India. Dust  $N_{CCN}$  of 100 to 200 cm<sup>-3</sup> appears over the Taklamakan desert region.

To verify the capability of ECLiAP retrieval to capture similar variability of particle physicochemical characteristics and its influence on CCN retrievals, we have investigated two distinct cases identified based on the variation in aerosol subtypes and meteorological variables. These scenarios are as follows: (1) Case-I: domination of polluted continental aerosols over southern India (red color box covered in figure 8) (2) Case-II: Mixture of polluted dust and polluted continental aerosols over northern India (blue color box covered in figure 8). The profiles of extinction coefficients at 532 nm and relative humidity, along with retrieved  $N_{CN}$  and  $N_{CCN}$  at six supersaturations, are presented in Figure 9. Figure 9a shows the profiles of the extinction coefficient at 532 nm and relative humidity for both cases. The extinction profile in case-I ranges from 0.7-1.2 km<sup>-1</sup>, is dominated by polluted continental aerosols in the high moisture condition (RH between 60%-80%), accumulates within the boundary layer ( $\sim 1.5$  km), and peaks at  $\sim 1.2$  km. Conversely, case-II represents the low moisture condition (RH  $\leq$  30%), with relatively large extinction coefficient values with a maximum of 1.6 km<sup>-1</sup> at  $\sim 0.2$  km altitude, influenced mainly by the mixture of polluted continental and polluted dust aerosols. These two cases are dynamically diverse and different in nature that providing a solid platform to verify the capability of ECLiAP in retrieving  $N_{CCN}$ . Figure 9b illustrates the retrieved  $N_{CN}$  using ECLiAP for both cases. The retrieved mean values of  $N_{CN}$  are observed to be almost similar ( $\sim 12000$  cm<sup>-3</sup> and  $\sim 11000$  cm<sup>-3</sup> for case-I and case-II, respectively). The profiles of  $N_{CN}$  follow a similar vertical distribution pattern of extinction coefficients. Figures 9c and 9d display the retrieved  $N_{CCN}$  at six supersaturations for Case-I and II, respectively. Interestingly,  $N_{CCN}$  values are found to be relatively lower in case-II, though its extinction coefficient is larger than in case-I. Note that ECLiAP considers polluted dust as a mixture of polluted continental and dust aerosol to retrieve  $N_{CCN}$ . The above-mentioned discrepancy can be only explained by the intrusion of dust and its non-hygroscopic behavior along

with dry conditions, further reducing the concentration of hygroscopic aerosols that leads to a decrease in  $N_{CCN}$ . This has been clearly reflected in the calculated activation ratio ( $AR = N_{CCN}/N_{CN}$ ) spectra in Figure S5. Figure S5 directly compares the AR spectra as a function of SS for both cases. The observed differences in the AR spectra reflect the nature of the particles to act as CCN. Relatively, larger values of AR in case-I indicate the dominance of hygroscopic aerosols get activated to CCN under high moisture and increase  $N_{CCN}$ . In contrast, the dust intrusion in case-II reduces the capability of particles to activate as CCN under low moisture and further reduces AR by ~20%-60% for the range of supersaturation from 0.07% to 1.0%. Given the limited sample space, the aim of the study is to demonstrate the potential of ECLiAP for retrieving reliable  $N_{CCN}$  data from spaceborne lidar measurements. We have adapted the retrieval approach to accommodate the available data, utilizing aerosol optical properties at two wavelengths and meteorological datasets. These modifications introduce potential limitations and uncertainties due to the availability of limited number of input parameters. While the CALIPSO case study offers valuable insights, we stress the need for further validation with independent measurements. A detailed comprehensive analysis comparing the CALIOP-retrieved  $N_{CCN}$  with multi-campaign airborne measurements is essential to evaluate the reliability of ECLiAP to construct the 3D CCN climatology at a global scale.

## 5 Discussion

Due to the absence of vertically resolved information in AOD, using it as a proxy for CCN in ACI studies has several shortcomings. Among other issues, a column property like AOD is not necessarily representative of  $N_{CCN}$  at altitudes, which affects the formation and growth of the cloud. Because no reliable global estimate of  $N_{CCN}$  exists, the fundamental assumptions of ACI cannot be robustly verified with the available sparse and localized in-situ measurements. In this study, we present a novel approach based on the  $3\beta+3\alpha$  technique for retrieving vertically-resolved cloud-relevant  $N_{CCN}$  from a single spaceborne lidar sensor. With this development, we demonstrate a new application of active satellite remote sensing that can provide direct measurements of CCN to improve understanding of ACI processes.

To address the problem of the non-uniqueness of a solution in the  $3\beta+2\alpha$  inverse technique, we have adopted a more realistic LUT-based approach using the  $3\beta+3\alpha$  multiwavelength technique, reflecting the bimodal particle distribution in the atmosphere better. Previous studies (Lv et al., 2018; Tan et al., 2019) demonstrated that CCN estimation is highly sensitive to the extinction coefficient than the backscatter coefficient. Therefore, leveraging the availability of derived extinction coefficients at 1064 nm as an additional input to ECLiAP to improve the retrieval accuracy of particle size distribution, particularly for coarse mode. In order to verify the performance, the CCN estimation error, using Eq. 12, has been calculated using both  $3\beta+2\alpha$  and  $3\beta+3\alpha$  techniques for each aerosol subtype in comparison to the observed CCN values. The relative difference in CCN estimation error between  $3\beta+2\alpha$  and  $3\beta+3\alpha$  techniques for each aerosol subtype is shown in Figure 10. The analysis shows that insertion of the  $\alpha_{1064}$  signal in the  $3\beta+3\alpha$  technique improves the CCN estimation by ~15% in total and ~20% for the coarse mode dominated

aerosol subtypes (i.e., marine and dust aerosols) compared to  $3\beta+2\alpha$ . The integration of derived product, along with direct lidar measurements, addresses the inherent non-uniqueness problem of inversion, and despite introducing uncertainties, the inclusion of extinction coefficient at 1064 nm significantly reduces retrieval uncertainty, emphasizing the value of additional lidar inputs in refining retrievals. Based on CCN closure analysis, Patel & Jiang, (2021) suggested that particle size and chemical composition are more crucial in the CCN activity at lower SS. In contrast, at higher SS, most particles become activated regardless of their size and composition. Therefore, the improvement in CCN estimation is relatively large in low SS ( $SS < 0.2\%$ ) than in high SS ( $SS > 0.2\%$ ). In our  $N_{CCN}$  retrieval approach, we use multiple input parameters: aerosol optical properties ( $\alpha_{355}$ ,  $\alpha_{532}$ ,  $\alpha_{1064}$ ,  $\beta_{355}$ ,  $\beta_{532}$ , and  $\beta_{1064}$ ) and relative humidity (RH). Each parameter plays a unique role in constraining aerosol size and concentration accurately. Through sensitivity analyses, we found that using all seven parameters leads to improved retrieval accuracy compared to a reduced set. The interplay between the parameters enhances the performance of algorithm, resulting in reliable and consistent  $N_{CCN}$  retrievals. The combination of aerosol optical properties and RH provides a comprehensive understanding of aerosol behavior, ensuring a more holistic characterization of aerosol properties in our study.

Systematic and random errors in the lidar measurements were evaluated individually and discussed in the sensitivity analysis. Both systematic and random errors realistically coexist in optical parameters, and therefore, we have evaluated their concurrent effect. The simulations were conducted with both systematic and random errors co-occurring. The results (not shown here) show that the retrieved CCN errors are much smaller than the error obtained individually by either systematic or random at each wavelength independently. The mean CCN error ranges between 7%-15% at SS from 0.07% to 1.0%. This retrieved CCN error is slightly large (~12%-18%) for the coarse-mode dominated aerosol subtypes (dust and marine). Summing up errors from multiple optical parameters might compensate for each other and improve the CCN retrievals. Furthermore, the retrieval from ECLiAP has few constraints. (i) it strongly depends on the accuracy of lidar-measured aerosol optical properties. The retrieval is only possible if the lidar signals are available at least at two wavelengths. (ii) the non-spherical shape of dust particles. While this study considers the spheroidal shape of dust particles, a recent study by Haarig et al., (2022) suggested that the assumption of spheroidal dust particle have limitations in obtaining an accurate particle depolarization ratio. Therefore, our assumption of spheroidal shape may not fully capture the complexity of dust particles and could lead to uncertainties in our dust-related retrieval. Although complex non-spherical shape models (Gasteiger et al., 2011; Saito et al., 2021) provide a more realistic representation of irregularly shaped dust particles, they are computationally expensive. We acknowledge this limitation and plan to explore alternative models in future studies. (iii) retrieval from ECLiAP is only performed for  $RH \leq 99\%$ . (iv) The use of mean refractive indices for each aerosol subtype in the creation of the look-up tables may limit the representation of refractive index variability within each subtype. This simplified approach reduces computation time but may compromise the accuracy of the LUTs in accounting for the full range of aerosol properties. (v) The CCN activity also depends on the mixing state, which is difficult to measure from space. Subsequently, an alternative solution is required to parametrize the effect of the mixing

state on CCN activity. (v) It is constrained by the inherent limitations of lidar measurements, which may not effectively capture particles with sizes smaller than 50 nanometers. Consequently, the algorithm does not fully account for the impact of new particle formation on the estimation of CCN concentrations.

The present study demonstrates the capability of ECLiAP to construct the three-dimensional global climatology of  $N_{CCN}$ . The global coverage of  $N_{CCN}$ , in conjunction with collocated retrieved cloud properties, will provide crucial input for the regional and global simulations that will provide realistic assessments of aerosol-induced cloud radiative forcing. The satellite-retrieved  $N_{CCN}$  can precisely separate the aerosols into natural and anthropogenic components, which can be further used for constraining aerosol emissions and transport models for air-quality studies. The application of detailed  $N_{CCN}$  will potentially mitigate the uncertainty of aerosol perturbed climate forcing (direct + indirect) and improve confidence in assessing anthropogenic contributions and climate change projections.

## 6 Summary

CCN number concentration is a critically-important parameter to constrain the relationship between aerosols and clouds and is needed to improve the understanding of ACI processes. The lack of direct measurements of CCN prevents robust testing of the underlying assumptions associated with aerosol-cloud interactions robustly and evaluates climate model simulations. In order to overcome this limitation, we presented ECLiAP, an emergent remote sensing-based analytical algorithm based on the physical law to retrieve the vertically resolved  $N_{CCN}$  from aerosol optical properties measured by the multiwavelength lidar system. Among the several fundamental aspects of the mathematical problem that must be solved during retrievals of microphysical parameters from multiwavelength lidar, the most crucial aspect is that the inverse solution is not unique. Therefore, the retrieval is implemented based on look-up tables generated from Mie scattering (and T-matrix/IGOM for dust particles) calculations. AERONET-based five representative aerosol subtypes with bimodal size distributions were considered. The influence of relative humidity on lidar-measured aerosol optical properties is corrected using the aerosol type-dependent hygroscopic growth factor to obtain the dry aerosol optical properties. As a tradeoff between the accuracy and computation time of the inversion, a successive approximation technique is utilized in two steps to retrieve the optically equivalent particle number size distribution. Once the aerosol size distribution parameters are obtained through the LUT, critical diameter and  $N_{CCN}$  at six supersaturations ranging from 0.07% to 1.0% is estimated using the  $\kappa$ -Köhler theory.

Sensitivity analyses were carried out to evaluate the algorithm performance and to show the influence of systematic and random errors of lidar-derived optical properties and auxiliary RH profiles on CCN retrieval. The performance of ECLiAP is evaluated with error-free data, and  $N_{CCN}$  at all six supersaturations is well reproduced with good accuracy and stability for the five aerosol subtypes. Systematic errors in extinction coefficients and RH greatly influence CCN retrieval errors. Reducing uncertainties in extinction coefficients effectively improves retrieval accuracy,

while uncertainties in backscatter coefficients benefit retrieval at higher SS. Differences in weights of fine- to coarse-mode particles within the aerosol subtypes lead to significant differences in the retrieval uncertainty. The differences can be explained via the weaker constraint of the algorithm for the coarse mode particles than for the fine mode. However, the insertion of the additional signal at a relatively longer wavelength reduced the differences in the retrieval uncertainty compared to previous techniques. The mean random errors are relatively small and found to be relatively large for the coarse mode-dominated aerosol subtypes, consistent with the sensitivities to the systematic errors. In realistic cases, systematic and random errors often offset each other and improve the mean CCN retrievals. Overall, the error analysis suggests that extinction coefficients at 355 and 532 nm must be reliably derived to ensure retrieval accuracy, including measurements at longer wavelengths further improve the CCN retrievals, particularly for the coarse mode-dominated aerosol subtypes.

The ECLiAP algorithm was applied to observational data from the NASA ORACLES airborne campaign to illustrate the potential of the algorithm.  $N_{CCN}$  retrieved from lidar (HSRL-2) measurements have been validated against the simultaneous measurements from the CCN counter installed in the flight. Considering the inhomogeneity in the vertical distribution of aerosols throughout the atmospheric column,  $N_{CCN}$  from in situ measurements and lidar retrievals agree well. Furthermore, for the first time, the ECLiAP has been applied to spaceborne lidar measurements – CALIOP/CALIPSO – to retrieve  $N_{CCN}$ . The results demonstrate that the  $N_{CCN}$  retrieved by ECLiAP is highly influenced by the variability of aerosol particle size and composition based on aerosol subtypes and also captures the meteorological influence. The vertically resolved information of aerosols, along with CCN from spaceborne lidar, is essential for investigating the ACI in detail.

Our future goals include a comprehensive evaluation of  $N_{CCN}$  derived from spaceborne lidar measurements, i.e., CALIOP/CALIPSO, with multi-campaign airborne measurements, covering various physicochemical regimes in the troposphere. The extensive validation will enable us to test the applicability of the ECLiAP algorithm in the context of estimating the  $N_{CCN}$  from space. Eventually, we plan to apply the ECLiAP algorithm over the period of CALIOP observations (~15 years) to generate the global three-dimensional  $N_{CCN}$  climatology. The data set coupled with the cloud-related data from the other satellite or state-of-the-art numerical models will help improve our understanding of the ACI. The science narrative of the NASA Aerosol and Cloud, Convection and Precipitation (ACCP) project pointed out that the combination of near-simultaneous and collocated lidar and polarimeter measurements can provide more detailed information regarding particle size, concentration, and composition (Braun et al., 2022). Therefore, our future work may also include combining the lidar measurements with passive observations in the ECLiAP algorithm to further narrow down the uncertainty of aerosol microphysics with the enhanced observational constraints (Xu et al., 2021), which will in turn improve the accuracy of CCN retrieval. Moreover, the ability of CALIOP to detect the aerosol subtypes has facilitated the retrieval of aerosol type-specific 3D  $N_{CCN}$  climatology on a global scale. These datasets from spaceborne lidar measurements will be beneficial for evaluating models and other satellite products, opening a new

window to investigate the region and regime-wise detailed ACI studies and better constraining anthropogenic contributions to the climate forcing in the climate model.

**Data availability statement.** All data that support the findings of this study are publicly available. The in-situ measurements at the ARM-SGP are available at <https://www.arm.gov/capabilities/observatories/sgp>.

All ORACLES data are accessible via the digital object identifiers (DOIs) provided under ORACLES science team.

references: [https://doi.org/10.5067/Suborbital/ORACLES/P3/2018\\_V2](https://doi.org/10.5067/Suborbital/ORACLES/P3/2018_V2) (ORACLES Science Team, 2020a), [https://doi.org/10.5067/Suborbital/ORACLES/P3/2017\\_V2](https://doi.org/10.5067/Suborbital/ORACLES/P3/2017_V2) (ORACLES Science Team, 2020b).

The CALIPSO data are available at <https://eosweb.larc.nasa.gov/>.

**Author contributions.** PNP conceptualized and designed the study. PNP carried out the data analysis and interpretation with contributions from JHJ, RG and HG. PNP wrote the manuscript. JHJ, RG, HG, OVK, MJG, LG, FX and OA reviewed, commented and/or edited the manuscript.

**Competing Interests:** The contact author has declared that none of the authors has any competing interests.

**Acknowledgment.** This work was conducted at the NASA-sponsored Jet Propulsion Laboratory (JPL), California Institute of Technology, under contract by NASA. We appreciate the facility provided by the JPL for data analysis and research. This work was supported by the NASA Postdoctoral Program, administered by Oak Ridge Associated Universities under contract with NASA. We are thankful to Charles A. Brock (Chemical Sciences Laboratory, National Oceanic and Atmospheric Administration, Boulder, CO, USA) for the fruitful discussion on the present study. All data were obtained from the Atmospheric Radiation Measurement (ARM) Program sponsored by the U.S. Department of Energy, Office of Science, Office of Biological and Environmental Research, Climate and Environmental Sciences Division, and National Science Foundation. We thank the ORACLES deployment support teams and the science team for a successful and productive mission. We thank the CALIPSO science team, for providing the CALIPSO data.

## References

- Andreae, M. O., & Rosenfeld, D. (2008). Aerosol-cloud-precipitation interactions. Part 1. The nature and sources of cloud-active aerosols. *Earth-Science Reviews*, 89(1–2), 13–41. <https://doi.org/10.1016/j.earscirev.2008.03.001>
- Bedoya-Velásquez, A. E., Navas-Guzmán, F., Granados-Muñoz, M. J., Titos, G., Román, R., Andrés Casquero-Vera, J., Ortiz-Amezcu, P., Antonio Benavent-Oltra, J., de Arruda Moreira, G., Montilla-



- 888 Rosero, E., Hoyos, C. D., Artiñano, B., Coz, E., Olmo-Reyes, F. J., Alados-Arboledas, L., & Guerrero-  
889 Rascado, J. L. (2018). Hygroscopic growth study in the framework of EARLINET during the SLOPE  
890 i campaign: Synergy of remote sensing and in situ instrumentation. *Atmospheric Chemistry and*  
891 *Physics*, 18(10), 7001–7017. <https://doi.org/10.5194/ACP-18-7001-2018>
- 892 Bi, L., Yang, P., Kattawar, G. W., & Kahn, R. (2009). Single-scattering properties of triaxial ellipsoidal  
893 particles for a size parameter range from the Rayleigh to geometric-optics regimes. *Applied Optics*,  
894 48(1), 114–126. <https://doi.org/10.1364/AO.48.000114>
- 895 Bohren, C. F., & Huffman, D. R. (1998). Absorption and Scattering of Light by Small Particles. *Absorption*  
896 *and Scattering of Light by Small Particles*. <https://doi.org/10.1002/9783527618156>
- 897 Bony, S., & Dufresne, J. L. (2005). Marine boundary layer clouds at the heart of tropical cloud feedback  
898 uncertainties in climate models. *Geophysical Research Letters*, 32(20), 1–4.  
899 <https://doi.org/10.1029/2005GL023851>
- 900 Braun, S., Stephens, G., Berndt, E., Blanchard, Y., Blanchet, J.-P., Carmichael, G., da Silva, A., Ferrare,  
901 R., Ivanco, M., Kacenelenbogen, M., Kirschbaum, D., Libois, Q., Mace, G., Omar, A., Petersen, W.,  
902 Redemann, J., Seidel, F., van den Heever, S., Waliser, D., & Winker, D. (2022). *Aerosol, Cloud,*  
903 *Convection, and Precipitation (ACCP) Science & Applications*.  
904 [https://aos.gsfc.nasa.gov/docs/ACCP\\_Science\\_Narrative-\(Mar2022\).pdf](https://aos.gsfc.nasa.gov/docs/ACCP_Science_Narrative-(Mar2022).pdf)
- 905 Brock, C. A., Wagner, N. L., Anderson, B. E., Attwood, A. R., Beyersdorf, A., Campuzano-Jost, P., Carlton,  
906 A. G., Day, D. A., Diskin, G. S., Gordon, T. D., Jimenez, J. L., Lack, D. A., Liao, J., Markovic, M.  
907 Z., Middlebrook, A. M., Ng, N. L., Perring, A. E., Richardson, M. S., Schwarz, J. P., ... Murphy, D.  
908 M. (2016). Aerosol optical properties in the southeastern United States in summer - Part 1:  
909 Hygroscopic growth. *Atmospheric Chemistry and Physics*, 16(8), 4987–5007.  
910 <https://doi.org/10.5194/ACP-16-4987-2016>
- 911 Burkart, J., Steiner, G., Reischl, G., & Hitzenberger, R. (2011). Long-term study of cloud condensation  
912 nuclei (CCN) activation of the atmospheric aerosol in Vienna. *Atmospheric Environment*, 45(32),  
913 5751–5759. <https://doi.org/10.1016/J.ATMOSENV.2011.07.022>
- 914 Burton, S. P., Chemyakin, E., Liu, X., Knobelspiesse, K., Stamnes, S., Sawamura, P., Moore, R. H.,  
915 Hostetler, C. A., & Ferrare, R. A. (2016). Information content and sensitivity of the  $3\beta + 2\alpha$  lidar  
916 measurement system for aerosol microphysical retrievals. *Atmospheric Measurement Techniques*,  
917 9(11), 5555–5574. <https://doi.org/10.5194/AMT-9-5555-2016>
- 918 Burton, S. P., Ferrare, R. A., Hostetler, C. A., Hair, J. W., Rogers, R. R., Obland, M. D., Butler, C. F., Cook,  
919 A. L., Harper, D. B., & Froyd, K. D. (2012). Aerosol classification using airborne High Spectral  
920 Resolution Lidar measurements-methodology and examples. *Atmospheric Measurement Techniques*,  
921 5(1), 73–98. <https://doi.org/10.5194/AMT-5-73-2012>
- 922 Burton, S. P., Hostetler, C. A., Cook, A. L., Hair, J. W., Seaman, S. T., Scola, S., Harper, D. B., Smith, J.  
923 A., Fenn, M. A., Ferrare, R. A., Saide, P. E., Chemyakin, E. V., & Müller, D. (2018). Calibration of  
924 a high spectral resolution lidar using a Michelson interferometer, with data examples from  
925 ORACLES. *Applied Optics*, 57(21), 6061. <https://doi.org/10.1364/AO.57.006061>
- 926 Carslaw, K. S., Boucher, O., Spracklen, D. v., Mann, G. W., L. Rae, J. G., Woodward, S., & Kulmala, M.  
927 (2010). A review of natural aerosol interactions and feedbacks within the Earth system. *Atmospheric*  
928 *Chemistry and Physics*, 10(4), 1701–1737. <https://doi.org/10.5194/ACP-10-1701-2010>

- 929 Chang, I., Gao, L., Burton, S. P., Chen, H., Diamond, M. S., Ferrare, R. A., Flynn, C. J., Kacenelenbogen,  
930 M., LeBlanc, S. E., Meyer, K. G., Pistone, K., Schmidt, S., Segal-Rozenhaimer, M., Shinozuka, Y.,  
931 Wood, R., Zuidema, P., Redemann, J., & Christopher, S. A. (2021). Spatiotemporal Heterogeneity of  
932 Aerosol and Cloud Properties Over the Southeast Atlantic: An Observational Analysis. *Geophysical*  
933 *Research Letters*, 48(7). <https://doi.org/10.1029/2020GL091469>
- 934 Chemyakin, E., Burton, S., Kolgotin, A., Müller, D., Hostetler, C., & Ferrare, R. (2016). Retrieval of aerosol  
935 parameters from multiwavelength lidar: investigation of the underlying inverse mathematical  
936 problem. *Applied Optics*, 55(9), 2188. <https://doi.org/10.1364/AO.55.002188>
- 937 Choudhury, G., & Tesche, M. (2022). Estimating cloud condensation nuclei concentrations from CALIPSO  
938 lidar measurements. *Atmospheric Measurement Techniques*, 15(3), 639–654.  
939 <https://doi.org/10.5194/AMT-15-639-2022>
- 940 Clarke, A., & Kapustin, V. (2010). Hemispheric aerosol vertical profiles: Anthropogenic impacts on optical  
941 depth and cloud nuclei. *Science*, 329(5998), 1488–1492.  
942 [https://doi.org/10.1126/SCIENCE.1188838/SUPPL\\_FILE/CLARKE.SOM.PDF](https://doi.org/10.1126/SCIENCE.1188838/SUPPL_FILE/CLARKE.SOM.PDF)
- 943 Coddington, O. M., Pilewskie, P., Redemann, J., Platnick, S., Russell, P. B., Schmidt, K. S., Gore, W. J.,  
944 Livingston, J., Wind, G., & Vukicevic, T. (2010). Examining the impact of overlying aerosols on the  
945 retrieval of cloud optical properties from passive remote sensing. *Journal of Geophysical Research*  
946 *Atmospheres*, 115(10). <https://doi.org/10.1029/2009JD012829>
- 947 Dubovik, O. (2002). Variability of absorption and optical properties of key aerosol types observed in  
948 worldwide locations. *J. Atmos. Sci.*, 59, 590–608. [https://doi.org/10.1175/1520-0469\(2002\)059<0590:voaaop>2.0.co](https://doi.org/10.1175/1520-0469(2002)059<0590:voaaop>2.0.co)
- 950 Dubovik, O., Sinyuk, A., Lapyonok, T., Holben, B. N., Mishchenko, M., Yang, P., Eck, T. F., Volten, H.,  
951 Muñoz, O., Veihelmann, B., van der Zande, W. J., Leon, J. F., Sorokin, M., & Slutsker, I. (2006).  
952 Application of spheroid models to account for aerosol particle nonsphericity in remote sensing of  
953 desert dust. *Journal of Geophysical Research Atmospheres*, 111(11).  
954 <https://doi.org/10.1029/2005JD006619>
- 955 Dusek, U., Frank, G. P., Hildebrandt, L., Curtius, J., Schneider, J., Walter, S., Chand, D., Drewnick, F.,  
956 Hings, S., Jung, D., Borrmann, S., & Andreae, M. O. (2006). Size matters more than chemistry for  
957 cloud-nucleating ability of aerosol particles. *Science*. <https://doi.org/10.1126/science.1125261>
- 958 Fan, J., Wang, Y., Rosenfeld, D., & Liu, X. (2016). Review of Aerosol–Cloud Interactions: Mechanisms,  
959 Significance, and Challenges. *Journal of the Atmospheric Sciences*, 73(11), 4221–4252.  
960 <https://doi.org/10.1175/JAS-D-16-0037.1>
- 961 Feingold, G., Yang, S., Hardesty, R. M., & Cotton, W. R. (1998). Feasibility of retrieving cloud  
962 condensation nucleus properties from doppler cloud radar, microwave radiometer, and lidar. *Journal*  
963 *of Atmospheric and Oceanic Technology*. [https://doi.org/10.1175/1520-0426\(1998\)015<1188:FORCCN>2.0.CO;2](https://doi.org/10.1175/1520-0426(1998)015<1188:FORCCN>2.0.CO;2)
- 965 Fernández, A. J., Molero, F., Becerril-Valle, M., Coz, E., Salvador, P., Artíñano, B., & Pujadas, M. (2018).  
966 Application of remote sensing techniques to study aerosol water vapour uptake in a real atmosphere.  
967 *Atmospheric Research*, 202, 112–127. <https://doi.org/10.1016/J.ATMOSRES.2017.11.020>
- 968 Gasteiger, J., Wiegner, M., Groß, S., Freudenthaler, V., Toledano, C., Tesche, M., & Kandler, K. (2011).  
969 Modelling lidar-relevant optical properties of complex mineral dust aerosols. *Tellus, Series B:*

970 *Chemical and Physical Meteorology*, 63(4), 725–741. <https://doi.org/10.1111/J.1600->  
971 0889.2011.00559.X

972 Ghan, S. J., & Collins, D. R. (2004). Use of in situ data to test a Raman lidar-based cloud condensation  
973 nuclei remote sensing method. *Journal of Atmospheric and Oceanic Technology*.  
974 [https://doi.org/10.1175/1520-0426\(2004\)021<0387:UOISDT>2.0.CO;2](https://doi.org/10.1175/1520-0426(2004)021<0387:UOISDT>2.0.CO;2)

975 Ghan, S. J., Rissman, T. A., Elleman, R., Ferrare, R. A., Turner, D., Flynn, C., Wang, J., Orgen, J., Hudson,  
976 J., Jonsson, H. H., VanReken, T., Flagan, R. C., & Seinfeld, J. H. (2006). Use of situ cloud  
977 condensation nuclei, extinction, and aerosol size distribution measurements to test a method for  
978 retrieving cloud condensation nuclei profiles from surface measurements. *Journal of Geophysical*  
979 *Research Atmospheres*, 111(5). <https://doi.org/10.1029/2004JD005752>

980 Giannakaki, E., Van Zyl, P. G., Müller, D., Balis, D., & Komppula, M. (2016). Optical and microphysical  
981 characterization of aerosol layers over South Africa by means of multi-wavelength depolarization and  
982 Raman lidar measurements. *Atmospheric Chemistry and Physics*, 16(13), 8109–8123.  
983 <https://doi.org/10.5194/ACP-16-8109-2016>

984 Gryspeerdt, E., & Stier, P. (2012). Regime-based analysis of aerosol-cloud interactions. *Geophysical*  
985 *Research Letters*. <https://doi.org/10.1029/2012GL053221>

986 Haarig, M., Ansmann, A., Engelmann, R., Baars, H., Toledano, C., Torres, B., Althausen, D., Radenz, M.,  
987 & Wandinger, U. (2022). First triple-wavelength lidar observations of depolarization and extinction-  
988 to-backscatter ratios of Saharan dust. *Atmospheric Chemistry and Physics*, 22(1), 355–369.  
989 <https://doi.org/10.5194/ACP-22-355-2022>

990 Hänel, A., Baars, H., Althausen, D., Ansmann, A., Engelmann, R., & Sun, J. Y. (2012). One-year aerosol  
991 profiling with EUCAARI Raman lidar at Shangdianzi GAW station: Beijing plume and seasonal  
992 variations. *Journal of Geophysical Research Atmospheres*, 117(13).  
993 <https://doi.org/10.1029/2012JD017577>

994 Hatch, T., & Choate, S. P. (1929). Statistical description of the size properties of non uniform particulate  
995 substances. *Journal of the Franklin Institute*, 207(3), 369–387. <https://doi.org/10.1016/S0016->  
996 0032(29)91451-4

997 IPCC. (2013). Working Group I Contribution to the IPCC Fifth Assessment Report, Climate Change 2013:  
998 The Physical Science Basis. *Ippc*, AR5(March 2013), 2014.  
999 <https://doi.org/10.1017/CBO9781107415324.Summary>

1000 IPCC. (2014). Climate Change 2014: Synthesis Report. Contribution of Working Groups I, II and III to the  
1001 Fifth Assessment Report of the Intergovernmental Panel on Climate Change. In *Core Writing Team*,  
1002 *R.K. Pachauri and L.A. Meyer*. IPCC. <https://doi.org/10.1017/CBO9781107415324.004>

1003 Jurányi, Z., Gysel, M., Weingartner, E., Decarlo, P. F., Kammermann, L., & Baltensperger, U. (2010).  
1004 Measured and modelled cloud condensation nuclei number concentration at the high alpine site  
1005 Jungfraujoch. *Atmospheric Chemistry and Physics*, 10(16), 7891–7906. <https://doi.org/10.5194/ACP->  
1006 10-7891-2010

1007 Kacarab, M., Lee Thornhill, K., Dobracki, A., Howell, S. G., O'Brien, J. R., Freitag, S., Poellot, M. R.,  
1008 Wood, R., Zuidema, P., Redemann, J., & Nenes, A. (2020). Biomass burning aerosol as a modulator  
1009 of the droplet number in the southeast Atlantic region. *Atmospheric Chemistry and Physics*, 20(5),  
1010 3029–3040. <https://doi.org/10.5194/ACP-20-3029-2020>

- 1011 Kantorovitch, L. (1939). The method of successive approximation for functional equations. *Acta*  
1012 *Mathematica*, 71(1), 63–97. <https://doi.org/10.1007/BF02547750>
- 1013 Kapustin, V. N., Clarke, A. D., Shinozuka, Y., Howell, S., Brekhovskikh, V., Nakajima, T., & Higurashi,  
1014 A. (2006). On the determination of a cloud condensation nuclei from satellite: Challenges and  
1015 possibilities. *Journal of Geophysical Research Atmospheres*. <https://doi.org/10.1029/2004JD005527>
- 1016 Kasten, F. (1969). Visibility forecast in the phase of pre-condensation. *Tellus*, 21(5), 631–635.  
1017 <https://doi.org/10.3402/TELLUSA.V21I5.10112>
- 1018 Kim, M. H., Omar, A. H., Tackett, J. L., Vaughan, M. A., Winker, D. M., Trepte, C. R., Hu, Y., Liu, Z.,  
1019 Poole, L. R., Pitts, M. C., Kar, J., & Magill, B. E. (2018). The CALIPSO version 4 automated aerosol  
1020 classification and lidar ratio selection algorithm. *Atmospheric Measurement Techniques*, 11(11),  
1021 6107–6135. <https://doi.org/10.5194/AMT-11-6107-2018>
- 1022 Koehler, K. A., Kreidenweis, S. M., DeMott, P. J., Petters, M. D., Prenni, A. J., & Carrico, C. M. (2009).  
1023 Hygroscopicity and cloud droplet activation of mineral dust aerosol. *Geophysical Research Letters*,  
1024 36(8). <https://doi.org/10.1029/2009GL037348>
- 1025 Kolmogorov, A. N. (1941). About the Logarithmic-normal Law of Particle Size Distribution during  
1026 Crushing. *Proceedings of the USSR Academy of Sciences*, 31(2), 99–101.
- 1027 Komppula, M., Mielonen, T., Arola, A., Korhonen, K., Lihavainen, H., Hyvärinen, A. P., Baars, H.,  
1028 Engelmann, R., Althausen, D., Ansmann, A., Müller, D., Panwar, T. S., Hooda, R. K., Sharma, V. P.,  
1029 Kerminen, V. M., Lehtinen, K. E. J., & Viisanen, Y. (2012). Technical Note: One year of Raman-  
1030 lidar measurements in Gual Pahari EUCAARI site close to New Delhi in India-Seasonal  
1031 characteristics of the aerosol vertical structure. *Atmospheric Chemistry and Physics*, 12(10), 4513–  
1032 4524. <https://doi.org/10.5194/ACP-12-4513-2012>
- 1033 Kuang, Y., Zhao, C., Tao, J., Bian, Y., Ma, N., & Zhao, G. (2017). A novel method for deriving the aerosol  
1034 hygroscopicity parameter based only on measurements from a humidified nephelometer system.  
1035 *Atmospheric Chemistry and Physics*, 17(11), 6651–6662. <https://doi.org/10.5194/ACP-17-6651-2017>
- 1036 Li, J., Liu, X., Yuan, L., Yin, Y., Li, Z., Li, P., Ren, G., Jin, L., Li, R., Dong, Z., Li, Y., & Yang, J. (2015).  
1037 Vertical distribution of aerosol optical properties based on aircraft measurements over the Loess  
1038 Plateau in China. *Journal of Environmental Sciences (China)*, 34, 44–56.  
1039 <https://doi.org/10.1016/J.JES.2015.01.021>
- 1040 Li, J., Yin, Y., Li, P., Li, Z., Li, R., Cribb, M., Dong, Z., Zhang, F., Li, J., Ren, G., Jin, L., & Li, Y. (2015).  
1041 Aircraft measurements of the vertical distribution and activation property of aerosol particles over the  
1042 Loess Plateau in China. *Atmospheric Research*, 155, 73–86.  
1043 <https://doi.org/10.1016/J.ATMOSRES.2014.12.004>
- 1044 Liu, J., & Li, Z. (2014). Estimation of cloud condensation nuclei concentration from aerosol optical  
1045 quantities: Influential factors and uncertainties. *Atmospheric Chemistry and Physics*, 14(1), 471–483.  
1046 <https://doi.org/10.5194/ACP-14-471-2014>
- 1047 Liu, P. F., Zhao, C. S., Göbel, T., Hallbauer, E., Nowak, A., Ran, L., Xu, W. Y., Deng, Z. Z., Ma, N.,  
1048 Mildnerberger, K., Henning, S., Stratmann, F., & Wiedensohler, A. (2011). Hygroscopic properties of  
1049 aerosol particles at high relative humidity and their diurnal variations in the north China plain.  
1050 *Atmospheric Chemistry and Physics*, 11(7), 3479–3494. <https://doi.org/10.5194/ACP-11-3479-2011>

1051 Liu, Z., Vaughan, M., Winker, D., Kittaka, C., Getzewich, B., Kuehn, R., Omar, A., Powell, K., Trepte, C.,  
 1052 & Hostetler, C. (2009). The CALIPSO lidar cloud and aerosol discrimination: Version 2 algorithm  
 1053 and initial assessment of performance. *Journal of Atmospheric and Oceanic Technology*, 26(7), 1198–  
 1054 1213. <https://doi.org/10.1175/2009JTECHA1229.1>

1055 Lv, M., Liu, D., Li, Z., Mao, J., Sun, Y., Wang, Z., Wang, Y., & Xie, C. (2017). Hygroscopic growth of  
 1056 atmospheric aerosol particles based on lidar, radiosonde, and in situ measurements: Case studies from  
 1057 the Xinzhou field campaign. *Journal of Quantitative Spectroscopy and Radiative Transfer*, 188, 60–  
 1058 70. <https://doi.org/10.1016/J.QSRT.2015.12.029>

1059 Lv, M., Wang, Z., Li, Z., Luo, T., Ferrare, R., Liu, D., Wu, D., Mao, J., Wan, B., Zhang, F., & Wang, Y.  
 1060 (2018). Retrieval of Cloud Condensation Nuclei Number Concentration Profiles From Lidar  
 1061 Extinction and Backscatter Data. *Journal of Geophysical Research: Atmospheres*, 123(11), 6082–  
 1062 6098. <https://doi.org/10.1029/2017JD028102>

1063 Mamouri, R. E., & Ansmann, A. (2016). Potential of polarization lidar to provide profiles of CCN-and INP-  
 1064 relevant aerosol parameters. *Atmospheric Chemistry and Physics*, 16(9), 5905–5931.  
 1065 <https://doi.org/10.5194/acp-16-5905-2016>

1066 Mattis, I., D'Amico, G., Baars, H., Amodeo, A., Madonna, F., & Iarlori, M. (2016). EARLINET Single  
 1067 Calculus Chain - Technical - Part 2: Calculation of optical products. *Atmospheric Measurement  
 1068 Techniques*, 9(7), 3009–3029. <https://doi.org/10.5194/AMT-9-3009-2016>

1069 Mishchenko, M. I., & Travis, L. D. (1998). Capabilities and limitations of a current FORTRAN  
 1070 implementation of the T-matrix method for randomly oriented, rotationally symmetric scatterers.  
 1071 *Journal of Quantitative Spectroscopy and Radiative Transfer*, 60(3), 309–324.  
 1072 [https://doi.org/10.1016/S0022-4073\(98\)00008-9](https://doi.org/10.1016/S0022-4073(98)00008-9)

1073 Molod, A., Takacs, L., Suarez, M., & Bacmeister, J. (2015). Development of the GEOS-5 atmospheric  
 1074 general circulation model: Evolution from MERRA to MERRA2. *Geoscientific Model Development*,  
 1075 8(5), 1339–1356. <https://doi.org/10.5194/GMD-8-1339-2015>

1076 Müller, D., Ansmann, A., Mattis, I., Tesche, M., Wandinger, U., Althausen, D., & Pisani, G. (2007).  
 1077 Aerosol-type-dependent lidar ratios observed with Raman lidar. *Journal of Geophysical Research  
 1078 Atmospheres*, 112(16). <https://doi.org/10.1029/2006JD008292>

1079 Müller, D., Böckmann, C., Kolgotin, A., Schneidenbach, L., Chemyakin, E., Rosemann, J., Znak, P., &  
 1080 Romanov, A. (2016). Microphysical particle properties derived from inversion algorithms developed  
 1081 in the framework of EARLINET. *Atmospheric Measurement Techniques*, 9(10), 5007–5035.  
 1082 <https://doi.org/10.5194/AMT-9-5007-2016>

1083 Müller, D., Mattis, I., Wandinger, U., Ansmann, A., Althausen, D., & Stohl, A. (2005). Raman lidar  
 1084 observations of aged Siberian and Canadian forest fire smoke in the free troposphere over Germany  
 1085 in 2003: Microphysical particle characterization. In *Journal of Geophysical Research D: Atmospheres*  
 1086 (Vol. 110, Issue 17). <https://doi.org/10.1029/2004JD005756>

1087 Müller, D., Wandinger, U., & Ansmann, A. (1999). Microphysical particle parameters from extinction and  
 1088 backscatter lidar data by inversion with regularization: theory. *Applied Optics*, 38(12), 2346.  
 1089 <https://doi.org/10.1364/AO.38.002346>

1090 Nam, C., Bony, S., Dufresne, J. L., & Chepfer, H. (2012). The too few, too bright tropical low-cloud  
1091 problem in CMIP5 models. *Geophysical Research Letters*, 39(21).  
1092 <https://doi.org/10.1029/2012GL053421>

1093 Omar, A. H., Winker, D. M., Kittaka, C., Vaughan, M. A., Liu, Z., Hu, Y., Trepte, C. R., Rogers, R. R.,  
1094 Ferrare, R. A., Lee, K. P., Kuehn, R. E., & Hostetler, C. A. (2009). The CALIPSO automated aerosol  
1095 classification and lidar ratio selection algorithm. *Journal of Atmospheric and Oceanic Technology*,  
1096 26(10), 1994–2014. <https://doi.org/10.1175/2009JTECHA1231.1>

1097 Paasonen, P., Asmi, A., Petäjä, T., Kajos, M. K., Äijälä, M., Junninen, H., Holst, T., Abbatt, J. P. D., Arneth,  
1098 A., Birmili, W., van der Gon, H. D., Hamed, A., Hoffer, A., Laakso, L., Laaksonen, A., Richard  
1099 Leaitch, W., Plass-Dülmer, C., Pryor, S. C., Räisänen, P., ... Kulmala, M. (2013). Warming-induced  
1100 increase in aerosol number concentration likely to moderate climate change. *Nature Geoscience*, 6(6),  
1101 438–442. <https://doi.org/10.1038/NGEO1800>

1102 Patel, P. N., Gautam, R., Michibata, T., & Gadhavi, H. (2019). Strengthened Indian Summer Monsoon  
1103 Precipitation Susceptibility Linked to Dust-Induced Ice Cloud Modification. *Geophysical Research  
1104 Letters*, 46(14), 8431–8441. <https://doi.org/10.1029/2018GL081634>

1105 Patel, P. N., & Jiang, J. H. (2021). Cloud condensation nuclei characteristics at the Southern Great Plains  
1106 site: role of particle size distribution and aerosol hygroscopicity. *Environmental Research  
1107 Communications*, 3(7), 075002. <https://doi.org/10.1088/2515-7620/AC0E0B>

1108 Patel, P. N., & Kumar, R. (2016). Dust Induced Changes in Ice Cloud and Cloud Radiative Forcing over a  
1109 High Altitude Site. *Aerosol and Air Quality Research*, 16(8), 1820–1831.  
1110 <https://doi.org/10.4209/aaqr.2015.05.0325>

1111 Patel, P. N., Quaas, J., & Kumar, R. (2017). A new statistical approach to improve the satellite-based  
1112 estimation of the radiative forcing by aerosol–cloud interactions. *Atmospheric Chemistry and Physics*,  
1113 17(5), 3687–3698. <https://doi.org/10.5194/acp-17-3687-2017>

1114 Pérez-Ramírez, D., Whiteman, D. N., Veselovskii, I., Kolgotin, A., Korenskiy, M., & Alados-Arboledas,  
1115 L. (2013). Effects of systematic and random errors on the retrieval of particle microphysical properties  
1116 from multiwavelength lidar measurements using inversion with regularization. *Atmospheric  
1117 Measurement Techniques*, 6(11), 3039–3054. <https://doi.org/10.5194/AMT-6-3039-2013>

1118 Petters, M. D., Carrico, C. M., Kreidenweis, S. M., Prenni, A. J., DeMott, P. J., Collett, J. L., & Moosmüller,  
1119 H. (2009). Cloud condensation nucleation activity of biomass burning aerosol. *Journal of Geophysical  
1120 Research Atmospheres*, 114(22), 1–16. <https://doi.org/10.1029/2009JD012353>

1121 Petters, M. D., & Kreidenweis, S. M. (2007). A single parameter representation of hygroscopic growth and  
1122 cloud condensation nucleus activity. *Atmospheric Chemistry and Physics*, 7(8), 1961–1971.  
1123 <https://doi.org/10.5194/ACP-7-1961-2007>

1124 Quaas, J., Boucher, O., Bellouin, N., & Kinne, S. (2008). Satellite-based estimate of the direct and indirect  
1125 aerosol climate forcing. *Journal of Geophysical Research Atmospheres*, 113(5).  
1126 <https://doi.org/10.1029/2007JD008962>

1127 Quaas, J., Ming, Y., Menon, S., Takemura, T., Wang, M., Penner, J. E., Gettelman, A., Lohmann, U.,  
1128 Bellouin, N., Boucher, O., Sayer, A. M., Thomas, G. E., McComiskey, A., Feingold, G., Hoose, C.,  
1129 Kristjánsson, J. E., Liu, X., Balkanski, Y., Donner, L. J., ... Schulz, M. (2009). Aerosol indirect effects

1130 - general circulation model intercomparison and evaluation with satellite data. *Atmospheric Chemistry*  
1131 *and Physics*, 9(22), 8697–8717. <https://doi.org/10.5194/acp-9-8697-2009>

1132 Redemann, J., Wood, R., Zuidema, P., Doherty, S. J., Luna, B., LeBlanc, S. E., Diamond, M. S., Shinozuka,  
1133 Y., Chang, I. Y., Ueyama, R., Pfister, L., Ryoo, J. M., Dobracki, A. N., da Silva, A. M., Longo, K.  
1134 M., Kacenelenbogen, M. S., Flynn, C. J., Pistone, K., Knox, N. M., ... Gao, L. (2021). An overview  
1135 of the ORACLES (ObseRvations of Aerosols above CLouds and their intERactionS) project: aerosol-  
1136 cloud-radiation interactions in the Southeast Atlantic basin. *Atmos. Chem. Phys.*, 21(3), 1507–1563.  
1137 <https://doi.org/10.5194/acp-21-1507-2021>

1138 Roberts, G. C., & Nenes, A. (2005). A continuous-flow streamwise thermal-gradient CCN chamber for  
1139 atmospheric measurements. *Aerosol Science and Technology*, 39(3), 206–221.  
1140 <https://doi.org/10.1080/027868290913988>

1141 Rose, D., Gunthe, S. S., Mikhailov, E., Frank, G. P., Dusek, U., Andreae, M. O., & Pöschl, U. (2008).  
1142 Calibration and measurement uncertainties of a continuous-flow cloud condensation nuclei counter  
1143 (DMT-CCNC): CCN activation of ammonium sulfate and sodium chloride aerosol particles in theory  
1144 and experiment. *Atmospheric Chemistry and Physics*, 8(5), 1153–1179. [https://doi.org/10.5194/ACP-](https://doi.org/10.5194/ACP-8-1153-2008)  
1145 [8-1153-2008](https://doi.org/10.5194/ACP-8-1153-2008)

1146 Rosenfeld, D. (2008). Flood or drought: how do aerosols affect precipitation? *Science*, 321, 1309–1313.

1147 Rosenfeld, D., Andreae, M. O., Asmi, A., Chin, M., Leeuw, G., Donovan, D. P., Kahn, R., Kinne, S.,  
1148 Kivekäs, N., Kulmala, M., Lau, W., Schmidt, K. S., Suni, T., Wagner, T., Wild, M., & Quaas, J.  
1149 (2014). Global observations of aerosol-cloud-precipitation- climate interactions. *Rev. Geophys.*, 52,  
1150 750–808. <https://doi.org/10.1002/2013RG000441>

1151 Rosenfeld, D., Zheng, Y., Hashimshoni, E., Pöhlker, M. L., Jefferson, A., Pöhlker, C., Yu, X., Zhu, Y., Liu,  
1152 G., Yue, Z., Fischman, B., Li, Z., Giguzin, D., Goren, T., Artaxo, P., Barbosa, H. M. J., Pöschl, U., &  
1153 Andreae, M. O. (2016). Satellite retrieval of cloud condensation nuclei concentrations by using clouds  
1154 as CCN chambers. *Proceedings of the National Academy of Sciences*.  
1155 <https://doi.org/10.1073/pnas.1514044113>

1156 Saito, M., Yang, P., Ding, J., & Liu, X. (2021). A Comprehensive Database of the Optical Properties of  
1157 Irregular Aerosol Particles for Radiative Transfer Simulations. *Journal of the Atmospheric Sciences*,  
1158 78(7), 2089–2111. <https://doi.org/10.1175/JAS-D-20-0338.1>

1159 Seinfeld, J. H., Bretherton, C., Carslaw, K. S., Coe, H., DeMott, P. J., Dunlea, E. J., Feingold, G., Ghan, S.,  
1160 Guenther, A. B., Kahn, R., Kraucunas, I., Kreidenweis, S. M., Molina, M. J., Nenes, A., Penner, J. E.,  
1161 Prather, K. A., Ramanathan, V., Ramaswamy, V., Rasch, P. J., ... Wood, R. (2016). Improving our  
1162 fundamental understanding of the role of aerosol–cloud interactions in the climate system.  
1163 *Proceedings of the National Academy of Sciences*, 113(21), 5781–5790.  
1164 <https://doi.org/10.1073/pnas.1514043113>

1165 Shinozuka, Y., Clarke, A. D., Nenes, A., Jefferson, A., Wood, R., McNaughton, C. S., Ström, J., Tunved,  
1166 P., Redemann, J., Thornhill, K. L., Moore, R. H., Latham, T. L., Lin, J. J., & Yoon, Y. J. (2015). The  
1167 relationship between cloud condensation nuclei (CCN) concentration and light extinction of dried  
1168 particles: Indications of underlying aerosol processes and implications for satellite-based CCN  
1169 estimates. *Atmospheric Chemistry and Physics*, 15(13), 7585–7604. [https://doi.org/10.5194/ACP-15-](https://doi.org/10.5194/ACP-15-7585-2015)  
1170 [7585-2015](https://doi.org/10.5194/ACP-15-7585-2015)

- Shipley, S. T., Tracy, D. H., Eloranta, E. W., Trauger, J. T., Sroga, J. T., Roesler, F. L., & Weinman, J. A. (1983). HIGH SPECTRAL RESOLUTION LIDAR TO MEASURE OPTICAL SCATTERING PROPERTIES OF ATMOSPHERIC AEROSOLS. 1: THEORY AND INSTRUMENTATION. *Applied Optics*, 22(23), 3716–3724. <https://doi.org/10.1364/AO.22.003716>
- Stier, P. (2016). Limitations of passive remote sensing to constrain global cloud condensation nuclei. *Atmospheric Chemistry and Physics*, 16(10), 6595–6607. <https://doi.org/10.5194/ACP-16-6595-2016>
- Tan, W., Zhao, G., Yu, Y., Li, C., Li, J., Kang, L., Zhu, T., & Zhao, C. (2019). Method to retrieve cloud condensation nuclei number concentrations using lidar measurements. *Atmospheric Measurement Techniques*, 12(7), 3825–3839. <https://doi.org/10.5194/AMT-12-3825-2019>
- Tesche, M., Ansmann, A., Müller, D., Althausen, D., Engelmann, R., Freudenthaler, V., & Groß, S. (2009). Vertically resolved separation of dust and smoke over Cape Verde using multiwavelength Raman and polarization lidars during Saharan Mineral Dust Experiment 2008. *Journal of Geophysical Research Atmospheres*, 114(13). <https://doi.org/10.1029/2009JD011862>
- Titos, G., Cazorla, A., Zieger, P., Andrews, E., Lyamani, H., Granados-Muñoz, M. J., Olmo, F. J., & Alados-Arboledas, L. (2016). Effect of hygroscopic growth on the aerosol light-scattering coefficient: A review of measurements, techniques and error sources. *Atmospheric Environment*, 141, 494–507. <https://doi.org/10.1016/J.ATMOSENV.2016.07.021>
- Torres, B., Dubovik, O., Fuertes, D., Schuster, G., Eugenia Cachorro, V., Lapyonok, T., Goloub, P., Blarel, L., Barreto, A., Mallet, M., Toledano, C., & Tanré, D. (2017). Advanced characterisation of aerosol size properties from measurements of spectral optical depth using the GRASP algorithm. *Atmospheric Measurement Techniques*, 10(10), 3743–3781. <https://doi.org/10.5194/AMT-10-3743-2017>
- Vaughan, M., Pitts, M., Trepte, C., Winker, D., Detweiler, P., Garnier, A., Getzewich, B., Hunt, W., Lamberth, J., Lee, K.-P., Lucker, P., Murray, T., Rodier, S., Tremas, T., Bazureau, A., & Pelon, J. (2017). *Cloud - Aerosol LIDAR Infrared Pathfinder Satellite Observations (CALIPSO), Data Management System, Data Products Catalog, Document No: PC-SCI-503, Release 4.10*. [https://doi.org/https://www-calipso.larc.nasa.gov/products/CALIPSO\\_DPC\\_Rev4x10.pdf](https://doi.org/https://www-calipso.larc.nasa.gov/products/CALIPSO_DPC_Rev4x10.pdf)
- Veselovskii, I., Dubovik, O., Kolgotin, A., Korenskiy, M., Whiteman, D. N., Allakhverdiev, K., & Huseynoglu, F. (2012). Linear estimation of particle bulk parameters from multi-wavelength lidar measurements. *Atmospheric Measurement Techniques*, 5(5), 1135–1145. <https://doi.org/10.5194/AMT-5-1135-2012>
- Veselovskii, I., Kolgotin, A., Griaiznov, V., Müller, D., Franke, K., & Whiteman, D. N. (2004). Inversion of multiwavelength Raman lidar data for retrieval of bimodal aerosol size distribution. *Applied Optics*, 43(5), 1180–1195. <https://doi.org/10.1364/AO.43.001180>
- Veselovskii, I., Kolgotin, A., Griaiznov, V., Müller, D., Wandinger, U., & Whiteman, D. N. (2002). Inversion with regularization for the retrieval of tropospheric aerosol parameters from multiwavelength lidar sounding. *Applied Optics*, 41(18), 3685. <https://doi.org/10.1364/AO.41.003685>
- Wang, Y., Li, Z., Zhang, Y., Du, W., Zhang, F., Tan, H., Xu, H., Fan, T., Jin, X., Fan, X., Dong, Z., Wang, Q., & Sun, Y. (2018). Characterization of aerosol hygroscopicity, mixing state, and CCN activity at a suburban site in the central North China Plain. *Atmospheric Chemistry and Physics*, 18(16), 11739–11752. <https://doi.org/10.5194/acp-18-11739-2018>



- 1211 Winker, D. M., Hunt, W. H., & McGill, M. J. (2007). Initial performance assessment of CALIOP.  
1212 *Geophysical Research Letters*, 34(19). <https://doi.org/10.1029/2007GL030135>
- 1213 Xu, F., Gao, L., Redemann, J., Flynn, C. J., Espinosa, W. R., da Silva, A. M., Stamnes, S., Burton, S. P.,  
1214 Liu, X., Ferrare, R., Cairns, B., & Dubovik, O. (2021). A Combined Lidar-Polarimeter Inversion  
1215 Approach for Aerosol Remote Sensing Over Ocean. *Frontiers in Remote Sensing*, 0, 2.  
1216 <https://doi.org/10.3389/FRSEN.2021.620871>
- 1217 Yang, P., Feng, Q., Hong, G., Kattawar, G. W., Wiscombe, W. J., Mishchenko, M. I., Dubovik, O., Laszlo,  
1218 I., & Sokolik, I. N. (2007). Modeling of the scattering and radiative properties of nonspherical dust-  
1219 like aerosols. *Journal of Aerosol Science*, 38(10), 995–1014.  
1220 <https://doi.org/10.1016/J.JAEROSCI.2007.07.001>
- 1221 Young, S. A., & Vaughan, M. A. (2009). The retrieval of profiles of particulate extinction from cloud-  
1222 aerosol lidar infrared pathfinder satellite observations (CALIPSO) data: Algorithm description.  
1223 *Journal of Atmospheric and Oceanic Technology*, 26(6), 1105–1119.  
1224 <https://doi.org/10.1175/2008JTECHA1221.1>
- 1225 Yu, H., Chin, M., Winker, D. M., Omar, A. H., Liu, Z., Kittaka, C., & Diehl, T. (2010). Global view of  
1226 aerosol vertical distributions from CALIPSO lidar measurements and GOCART simulations:  
1227 Regional and seasonal variations. *Journal of Geophysical Research Atmospheres*, 115(4), 1–19.  
1228 <https://doi.org/10.1029/2009JD013364>

1229

1230

**Table 1:** Typical parameter ranges for the aerosol bimodal distribution used in our study to construct the LUTs.  $V_f^t / V_c^t$  is the ratio of the volume concentration of the fine mode to the coarse mode.  $m_R$  and  $m_I$  represent the mean values of real and imaginary parts of the complex refractive index.

Aerosol Parameters	Marine	Dust	Polluted Continental	Clean Continental	Biomass burning
$r_f^v$	0.065-0.085	0.062-0.082	0.075-0.095	0.08-0.11	0.072-0.082
$r_c^v$	0.5-0.6	0.59-0.64	0.6-0.71	0.42-0.52	0.75-0.80
$\sigma_f^v$	0.46-0.54	0.4-0.53	0.38-0.46	0.37-0.45	0.4-0.47
$\sigma_c^v$	0.68-0.78	0.6-0.7	0.65-0.75	0.70-0.80	0.65-0.75
$V_f^t / V_c^t$	0.1-0.25	0.1-0.5	1.0-2.0	0.01-0.15	1.5-2.5
$m_R / m_I$	1.36/0.0015	1.56/0.001	1.47/0.014	1.401/0.003	1.51/0.021
$\kappa$	0.7	0.03	0.27	0.31	0.1

**Table 2:** CCN errors at six supersaturation (SS) retrieved from error-free inputs for the five aerosol types

Aerosol Types	CCN error (%)					
	0.07%	0.1%	0.2%	0.4%	0.8%	1.0%
Marine	-0.00 ± 0.21	-0.01 ± 0.23	0.00 ± 0.26	-0.00 ± 0.25	0.00 ± 0.23	-0.00 ± 0.24
Dust	-0.01 ± 0.22	-0.01 ± 0.23	0.00 ± 0.26	-0.01 ± 0.24	0.00 ± 0.25	-0.01 ± 0.23
Mean ± SD (%) Polluted continental	-0.01 ± 0.18	0.00 ± 0.18	-0.01 ± 0.16	0.00 ± 0.18	-0.01 ± 0.19	-0.00 ± 0.18
Clean continental	-0.01 ± 0.19	-0.01 ± 0.20	-0.01 ± 0.19	-0.00 ± 0.17	-0.00 ± 0.18	-0.01 ± 0.17
Smoke	-0.01 ± 0.19	-0.01 ± 0.21	-0.01 ± 0.18	-0.01 ± 0.20	-0.00 ± 0.22	-0.01 ± 0.19

1239

1240

1241

***Table 3:** Sensitivity of CCN retrieval to the bimodal fits at different supersaturation ratios from the 100 aerosol size distributions obtained from ARM-SGP. The CCN error is calculated as an absolute value.*

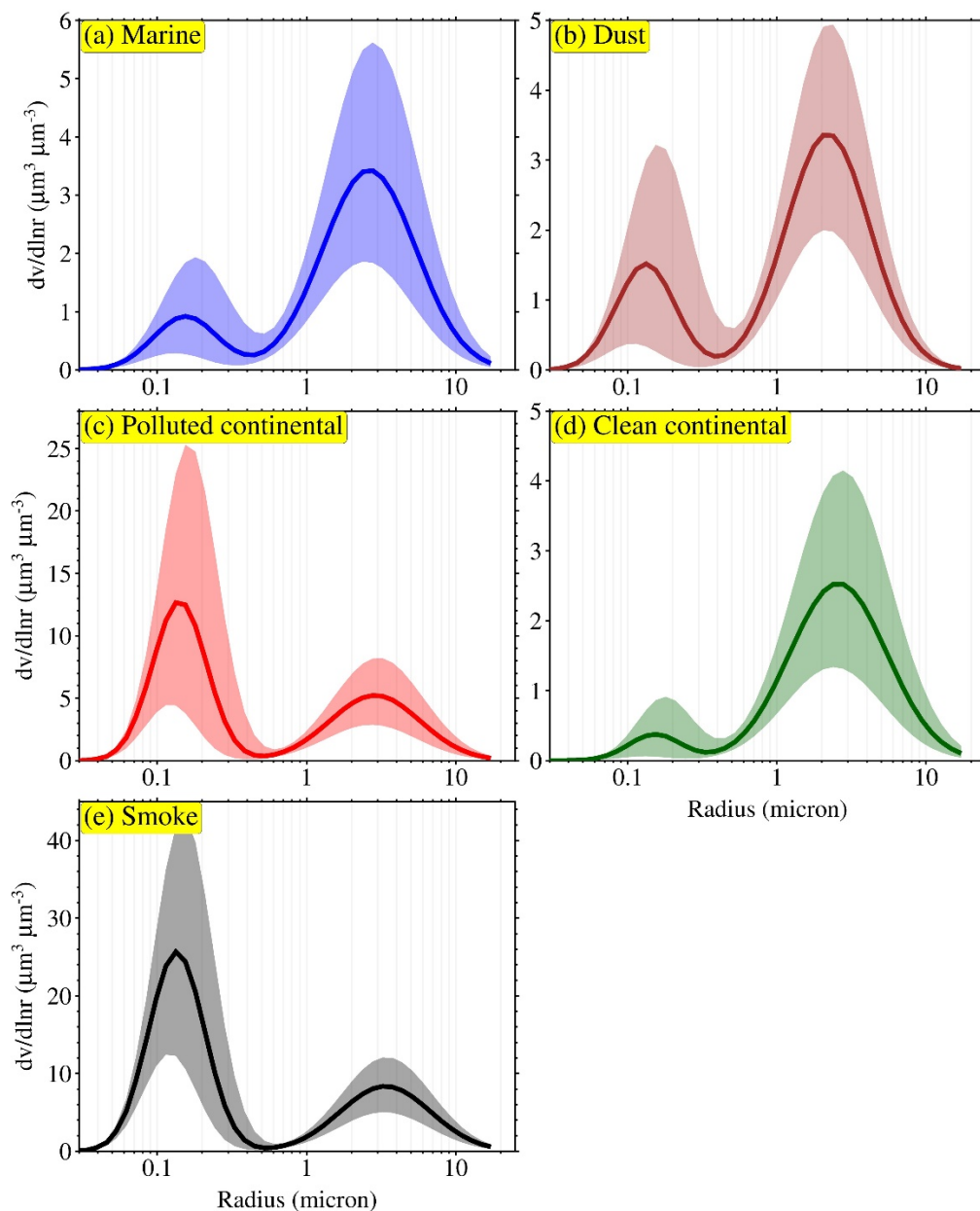
1242

1243

	CCN error (%)					
	0.07%	0.1%	0.2%	0.4%	0.8%	1.0%
Mean ± SD (%)	3.3 ± 2.4	3.9 ± 2.8	3.1 ± 2.7	2.9 ± 1.8	2.1 ± 1.5	1.7 ± 1.3

1244

1245



1247  
 1248 **Figure 1: Bimodal log-normal particle size distributions** for five aerosol types (marine, dust,  
 1249 polluted continental, clean continental and smoke aerosols) considered in this study to build the  
 1250 look-up-tables (LUTs). These particle size distributions were derived using measurements from  
 1251 sun/sky radiometer at multiple selected Aerosol Robotic Network (AERONET) sites. Solid line  
 1252 represents the mean of particle size distribution, whereas the shaded area shows the range of size  
 1253 distribution covers in the respective LUTs.

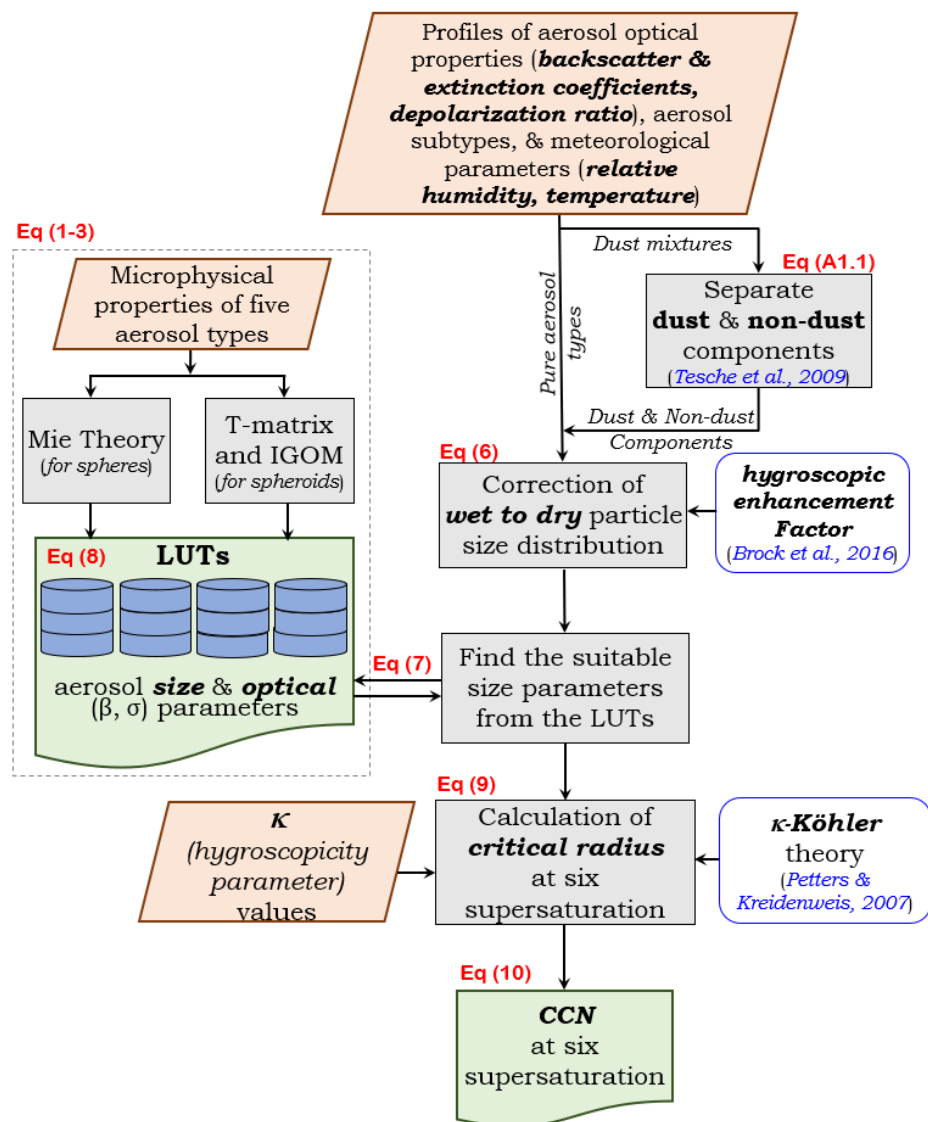
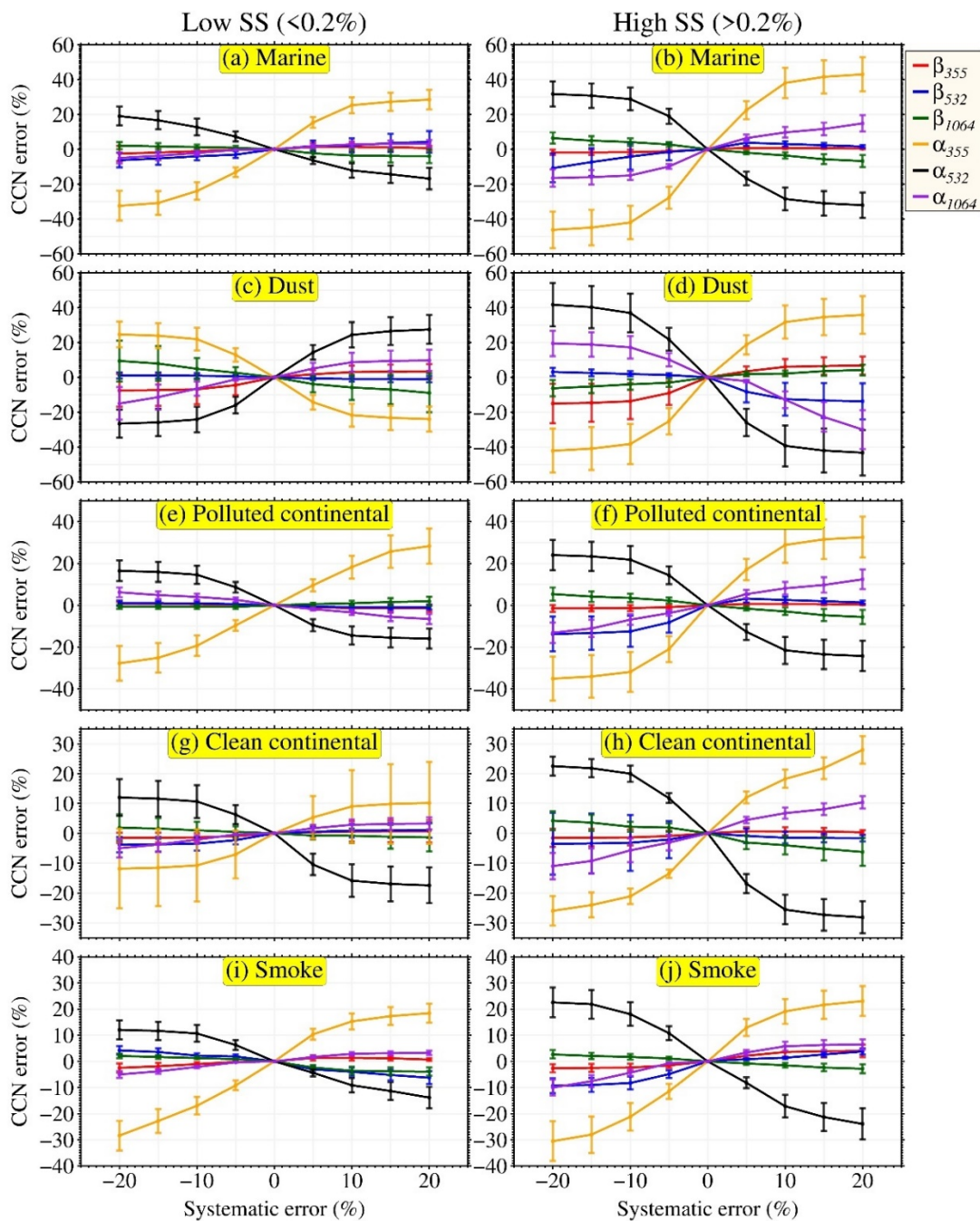


**Figure 2: Flowchart of ECLiAP algorithm for the retrieval of  $N_{CCN}$  from lidar measurements.** The steps within the dotted line box describes the pre-processing which includes the calculation of aerosol optical properties using Mie scattering theory (T-matrix/IGOM for dust) to build look-up-tables for five aerosol models. The steps outside the dotted line box represent the retrieval process of  $N_{CCN}$  from the given inputs of aerosol optical properties and meteorological parameters. The chart also refers to the used equations associated to the particular retrieval process.



1264

1265

1266

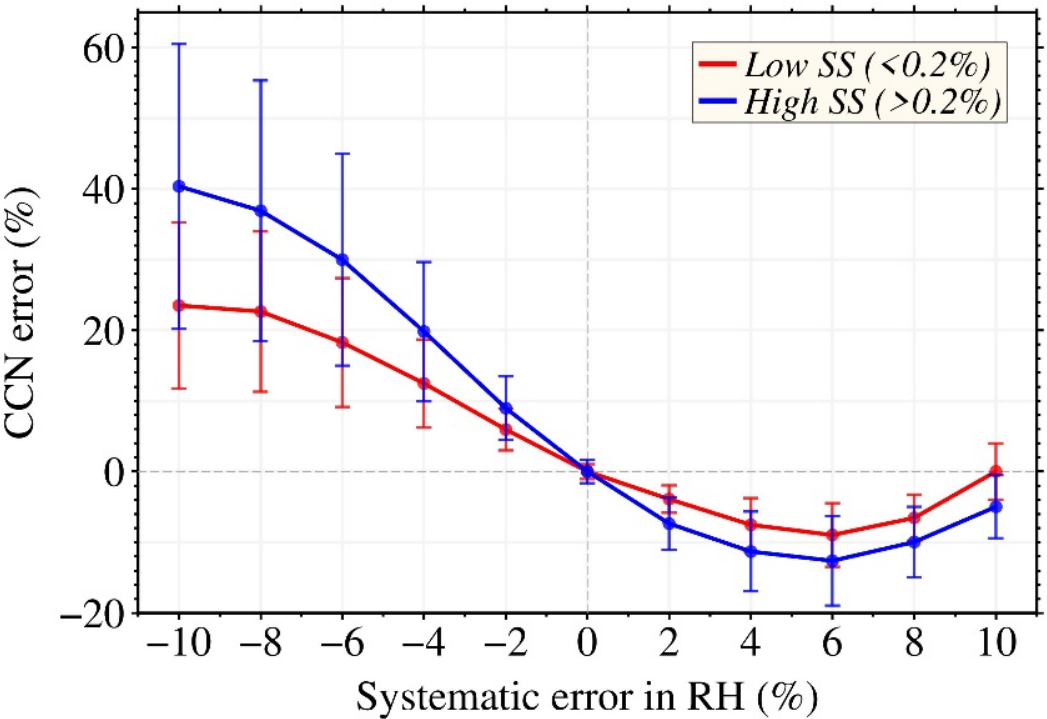
1267

1268

**Figure 3: Systematic errors in retrieved  $N_{CCN}$ .** This represent the errors in retrieved  $N_{CCN}$  as a function of systematic errors in backscatter and extinction coefficients at all three wavelengths for low ( $\leq 0.2\%$ ) and high ( $> 0.2\%$ ) supersaturations and for all five aerosol subtypes as. The markers denote the mean value and the error bars represent the standard deviation.

1269

1270



1271

1272

1273

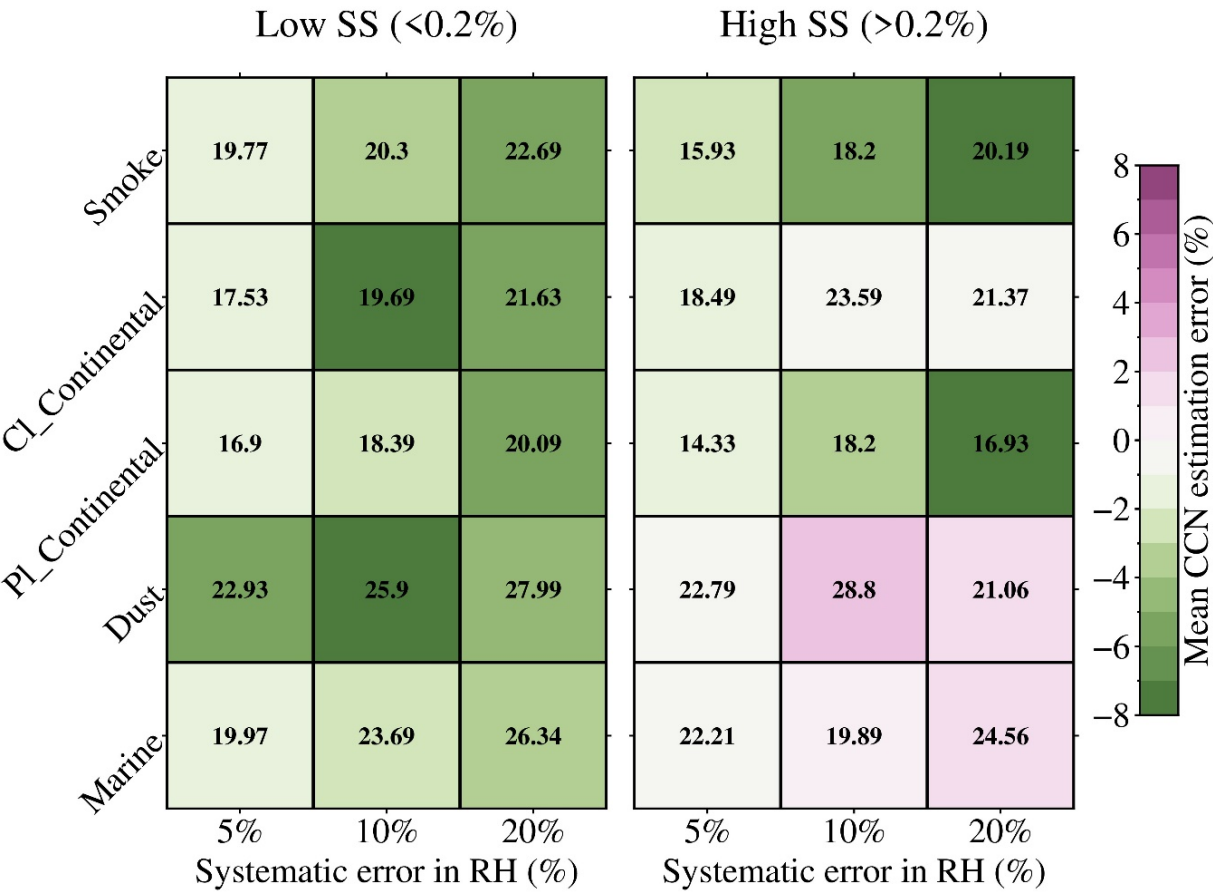
1274

1275

**Figure 4: Systematic errors in retrieved  $N_{CCN}$ .** This represent the errors in retrieved  $N_{CCN}$  as a function of systematic error in RH, combines for all aerosol subtypes, at low ( $\leq 0.2\%$ ) and high ( $> 0.2\%$ ) supersaturations. The markers denote the mean value and the error bars represent the standard deviation.

1276

1277



1278

1279

1280

1281

1282

1283

**Figure 5: Random errors in retrieved  $N_{CCN}$ .** This represents the random errors in retrieved  $N_{CCN}$  at low ( $\leq 0.2\%$ ) and high ( $> 0.2\%$ ) supersaturations with different random error conditions individually for five aerosol subtypes. The uncertainty of backscatter and extinction coefficients off all the tests is 10% and the uncertainties of RH are 5%, 10% and 20%. The color shows the mean values whereas number shows the  $\pm 1$  standard deviation of errors.



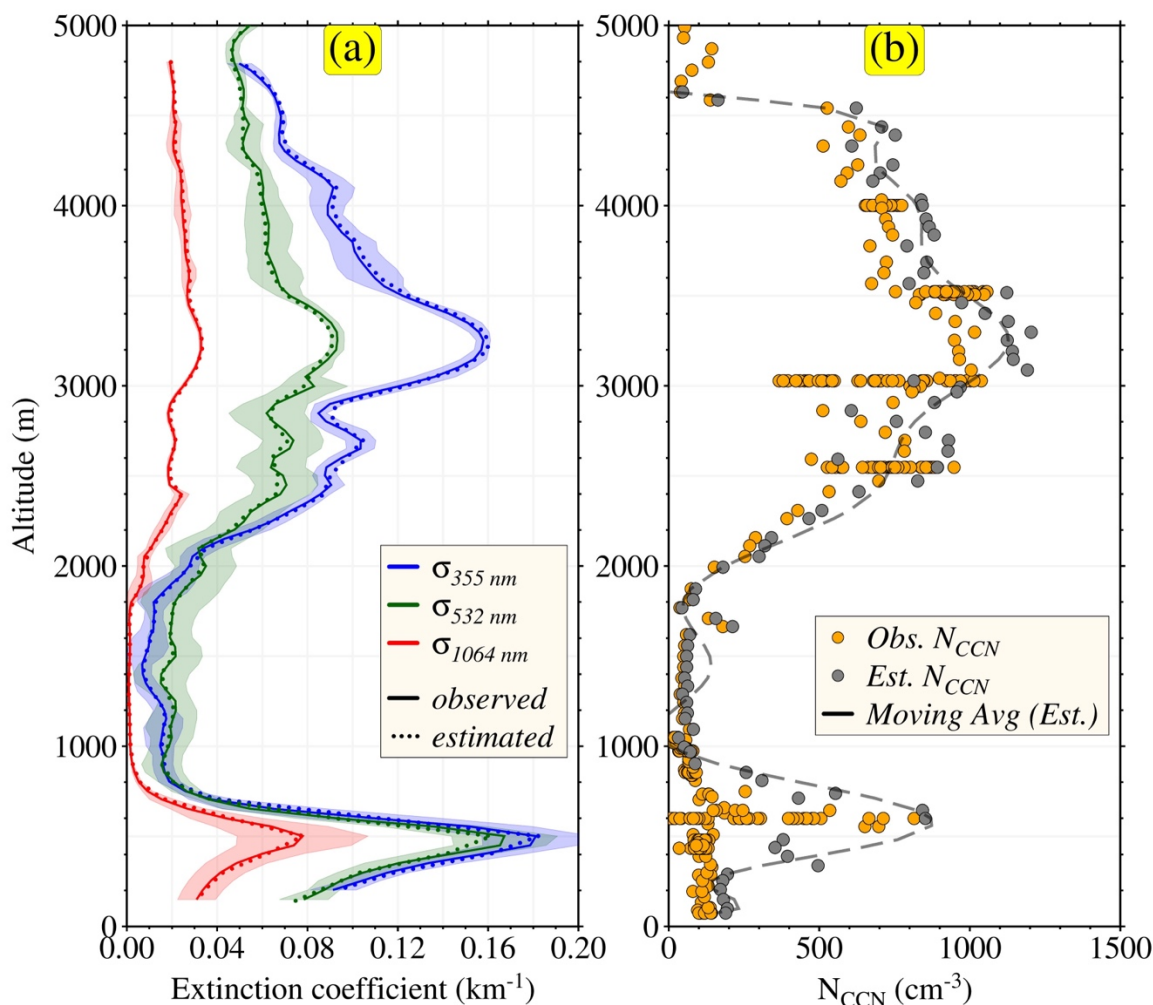
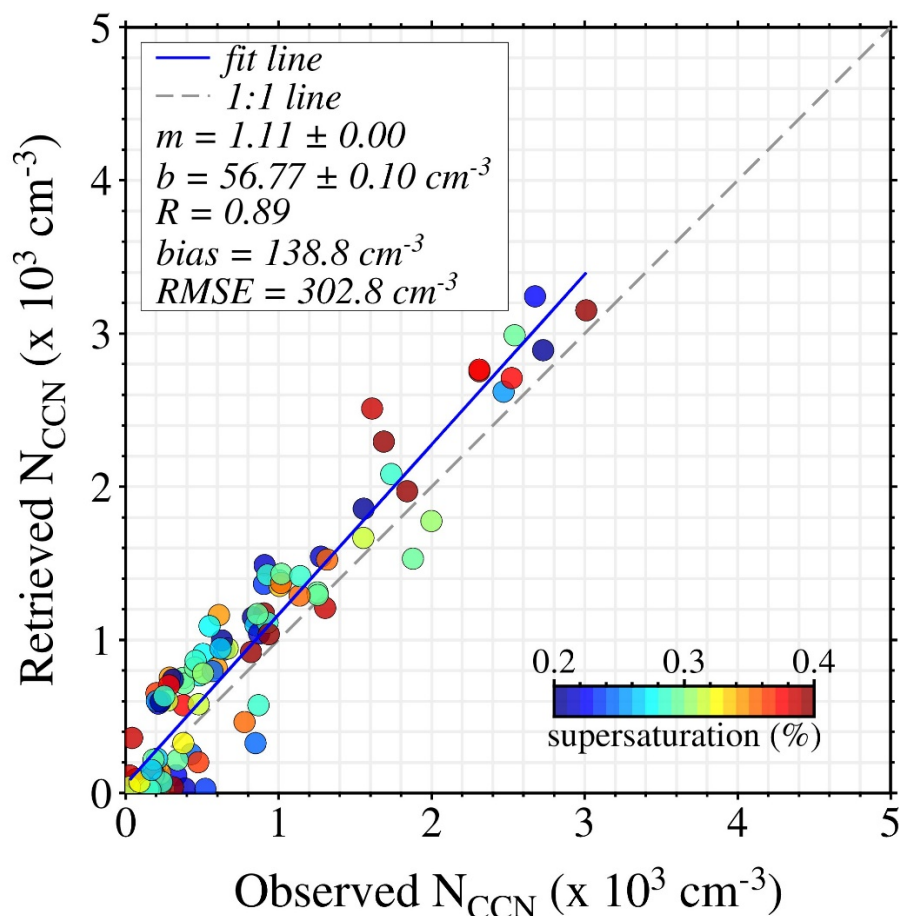


**Figure 6: Comparison between retrieved and observed vertical profiles of aerosol extinction coefficients and  $N_{\text{CCN}}$ .** The ECLiAP retrieved (a) aerosol extinction coefficients at 355, 532 and 1064 nm and (b)  $N_{\text{CCN}}$  were compared against the one observed during NASA ORACLES airborne campaign. The lidar signals were mainly influenced by the mixture of smoke and dust or marine aerosols. The relationship between HSRL-2 measured aerosol extinction coefficients (solid lines) and retrieved (dotted line) by an algorithm in the left panel. The right panel illustrates the comparison of retrieved  $N_{\text{CCN}}$  using lidar measurements and measured by CCN counter. The dashed line in the right panel shows the moving average of retrieved  $N_{\text{CCN}}$  values. CCN counter measured  $N_{\text{CCN}}$  at supersaturation ranging from 0.32%-0.34% for the selected region (described in Figure S4), therefore, the retrieval of  $N_{\text{CCN}}$  was carried out at supersaturation of 0.34%.

1297

1298



1299

1300 **Figure 7: Comparison between retrieved and observed  $N_{CCN}$ .** The comparison between ECLiAP  
 1301 retrieved  $N_{CCN}$  from HSRL-2 lidar measurements and the measured  $N_{CCN}$  values from CCN  
 1302 counter. The HSRL-2 and CCN counter data were collected from the multiple flights during NASA-  
 1303 ORACLES airborne campaigns conducted in 2017-2018. The color bar displays the observed  
 1304 values of supersaturation for each measurement and the  $N_{CCN}$  were retrieved on the same  
 1305 supersaturation for the direct comparison. The slope and intercept of the best fit line are given in  
 1306 the key by  $m$  and  $b$ , respectively. The gray dash line indicates the unit slope line and blue solid  
 1307 line indicates the regression line.

1308

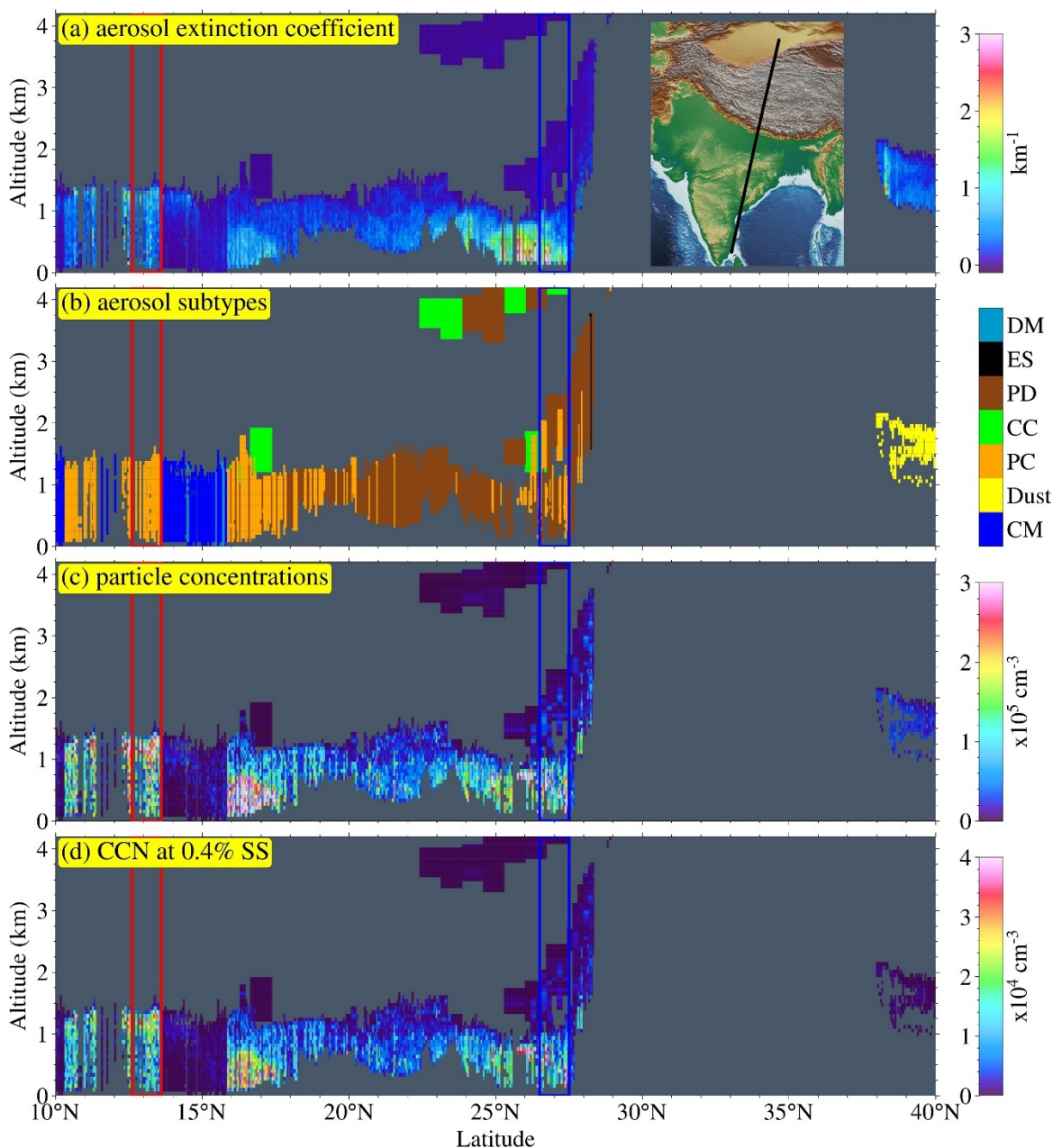
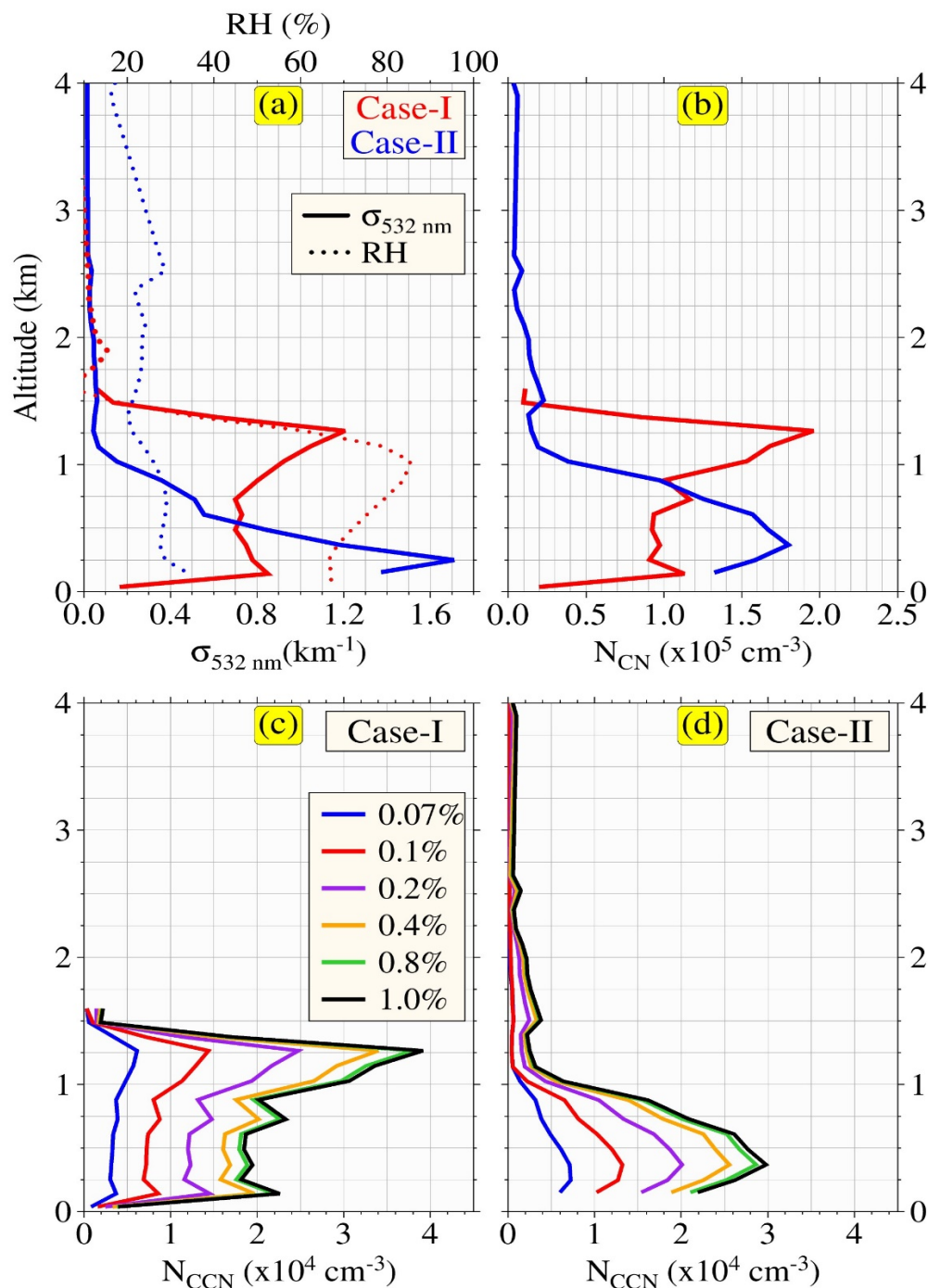


**Figure 8: Retrieval from spaceborne lidar measurements.** Explore the capability of ECLiAP, the  $N_{CN}$ , and  $N_{CCN}$  retrieved from CALIOP onboard CALIPSO observations on 01 January 2019, passing over the Tibetan plateau and Indian landmass. CALIOP derived (a) extinction coefficient at 532 nm, (b) aerosol subtypes were shown in the upper two panels. The lower two panels illustrate the ECLiAP retrieved (c) total particle concentrations ( $N_{CN}$ ), and (d)  $N_{CCN}$  at supersaturation 0.4%. The two color boxes in red (case-I) and blue (case-II) are the two different scenarios that are further studied to assess the capability of ECLiAP.



1319

1320

1321

1322

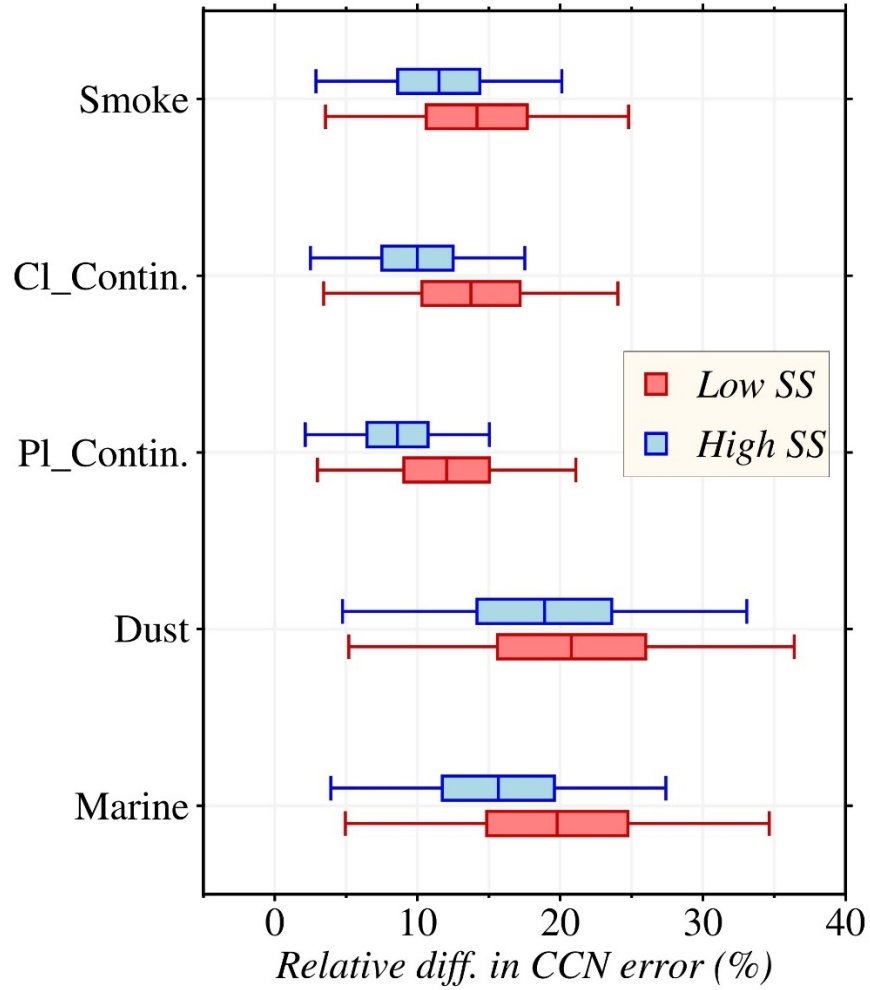
1323

1324

**Figure 9: Case studied from CALIOP observations.** As per mentioned above, two different scenarios (case-I dominated by polluted continental and case-II contains a mixture of polluted continental and polluted dust) were identified and studied in detail to assess the potential of ECLiAP to accurately capture the particles physicochemical characteristics and their influence on the retrieved values along with meteorological influence.

1325

1326



1327

1328 **Figure 10: Relative difference in CCN error between  $3\beta+2\alpha$  and  $3\beta+3\alpha$ .** The CCN error were  
 1329 calculated against the given inputs using Eq. (11) for both the  $3\beta+2\alpha$  and  $3\beta+3\alpha$  techniques  
 1330 individually. Later the relative difference of CCN error has calculated from the individual CCN  
 1331 errors at low and high supersaturations for each aerosol subtypes.